

Neural Networks as Globally Optimal Multilayer Convolution Architectures for Learning Fluid Flows

Shivakanth Chary Puligilla · Balaji Jayaraman

Received: date / Accepted: date

Abstract In this work we explore globally optimal multilayer convolution models such as feed forward neural-networks (FFNN) for learning and predicting dynamics from transient fluid flow data. While machine learning in general depends on data quality relative to the underlying dynamics of the system, it is important for a given data-driven learning architecture to make the most of this available information. To this end, we cast the suite of recently popular data-driven learning approaches that approximate the Markovian dynamics through a linear model in a higher-dimensional feature space as a multilayer architecture similar to neural networks, but with layer-wise locally optimal convolution mappings. As a contrast, we also represent the traditional neural networks with some slight modifications as a multilayer architecture, but with convolution maps optimized in response to the global learning cost (i.e. not the cost of learning across two immediate layers). We show through examples of data-driven learning of canonical fluid flows that globally optimal FFNN-like methods owe their success to leveraging the extended learning parameter space available in multilayer models to achieve a common goal of minimizing the training cost function while incorporating nonlinear function maps between layers. On the other hand, locally optimal multilayer models also show improvement from the same factors, but behave like shallow neural networks requiring much larger hidden layers to achieve comparable learning and prediction accuracy. We illustrate these ideas by learning the dynamics from snapshots of training data and predicting the temporal evolution of canonical nonlinear fluid flows including the limit-cycle attractor in a cylinder wake and the instability-driven dynamics of buoyant Boussinesq flow. Locally optimal methods allow for forward and backward convolutions, the globally optimal FFNNs can only handle forward maps which prevents their use as Koopman approximation tools .

Keywords model order reduction; reduced order modeling, DMD, extended DMD and feed forward neural networks

PACS

1 Introduction

Fluid flows are predominantly multiscale phenomena occurring over a wide range of length and time scales such as transition [1], turbulence [2] and flow separation [3]. Direct numerical simulation (DNS) of such realistic high Reynolds number flows even in their canonical forms is a challenge even with current computing capacity. On the other hand, advances in experimental techniques for visualization and data acquisition have led to an abundance of fluid flow measurement data, but these measurements are often sparse and in many cases the underlying phenomenology or governing model is not known. In both these cases, there is a need for efficient data-driven models to serve the twin goals of system modulation to achieve desired effects, i.e. flow control [4, 5] or forecasting for improved and informed decision making[6, 7, 8] or both. Additionally, data-driven models also allow for extraction of dynamical and physical characteristics to generate novel insight [9, 10] of the system behavior. In flow control applications linear operator based control is often preferred due to the sheer volume of available expertise and their past success[11] although nonlinear operator

Shivakanth chary Puligilla
School of Mechanical and Aerospace Engineering, Oklahoma State University, Stillwater, OK, USA
E-mail: shivakanthchary.puligilla@okstate.edu

Balaji Jayaraman (Corresponding Author)
School of Mechanical and Aerospace Engineering, Oklahoma State University, Stillwater, OK, USA
E-mail: balaji.jayaraman@okstate.edu

based flow control is an emerging area of research. Consequently, learning a linear system model from data is often preferred. The vast amount of recent literature [12,13] including that from our team [14] addresses this broad area of need, but do not perform adequately in data-sparse situations. In this paper, we explore nonlinear machine learning frameworks that are capable of overcoming this limitation for canonical fluid flows. Particular for this article, we explore bluff body wake flows and buoyancy-driven mixing.

A good data-driven model should perform well in both system identification and prediction using limited amounts of data. In addition, these models need to be computationally tractable which makes dimensionality reduction essential. System identification enables learning of stability and flow characteristics such as unstable modes and coherent structures for the purposes of understanding the flow. For example, proper orthogonal decomposition (POD) [15] via singular value decomposition (SVD) [16] and its close cousin, the Dynamic mode decomposition (DMD) [12] are well known methods to extract such relevant spectral information. However, the capacity of DMD for long-term prediction is underwhelming [17]. POD-based methods that use Galerkin projection onto the flow governing equations are more successful, but require knowledge of the system. In this study, we focus on purely data-driven scenarios without knowledge of governing equations. By long-time predictions, we imply evolving the system model over multiple characteristic time-scales beyond the training regime. The other type is to employ the model to predict different system trajectories which is commonly referred using the generic term *forecasting*. Obviously, the precise definition of the ‘long-time’ prediction or forecasting depends on the flow physics of interest. For example, a limit-cycle system evolving on a stable attractor will be more amenable to forecasting from limited data as compared to more complex nonlinear mixing dynamics. In the case of cylinder wake flow explored in this study, forecasting represent predicting the limit cycle [18,19] dynamics using limited data in the transient region. We explore such cases as they are sensitive to error growth and hence, used to evaluate a given model. Errors in model learning can be attributed to limited training data, measurement noise, model overfitting and insufficient validation [20,21]. The contributions from this paper are highly relevant within this context as we systematically explore and assess how nonlinear regression-based data-driven models perform relative to commonly used linear regression-based models for dynamically evolving fluid flows.

There are two classes of approaches for modeling dynamical systems from limited data, namely Markov and non-Markov models. For a given current state \mathbf{x}_t and future state \mathbf{x}_{t+T} of a dynamical system, a Markov model [22], under some transformation g, h , evolves the system state as $g(\mathbf{x}_{t+T}) = \mathcal{K}h(\mathbf{x}_t)$. Learning such an operator \mathcal{K} is a key component of building such a model. We consider a Markovian process to be minimally memory dependent and popular approaches for modeling such systems include dynamic mode decomposition (DMD) [12,10] and Feed forward neural networks (FFNN). Recently, many of the linear operator [11,23, 13,14] methods for modeling nonlinear dynamics have been shown to be generalizable into a Koopman operator [24] theoretic framework. The Koopman approximation-based methods can be considered as a special case of Markov models if the transformations ($g = h$) to the feature space are identical. On the other hand, if the model incorporates history (or copious amounts of memory) of the state variables to predict a future state, then it is considered non-Markovian. Recurrent neural networks(RNN) are good examples of non-Markovian models and have been employed for learning dynamical systems both in the past [25,26] and in recent times [27,28]. Although these have shown success, they are very hard to build and train [29] as compared to standard feed forward neural networks (FFNNs) [30]. This is because, the standard backpropagation-based algorithms introduce overfitting and the longer training times can lead to exploding or vanishing gradient problems.

While Markov models are popular, especially the linear variants, their success is often tied to two aspects: (i) the ability of the projection or convolutions to the feature space [11,31,14] to accurately map data without loss of information while incorporating the appropriate degree of nonlinearity and (ii) their ability to capture the evolution of the dynamics in the feature space [14]. This renders many such learning methodologies into an exercise in identifying the optimal ‘magic’ feature maps. A common approach to building such nonlinear convolution operators is to layer multiple ‘elementary’ convolutions [14]. While DMD [12,10] employs a single-layer convolution operator based on singular value decomposition (SVD) of the training data, its multilayer variant EDMD [13] incorporates a second convolution (over a layer of SVD convolution) by embedding nonlinear functions. This approach is effective if one knows the nature of the nonlinearity *a priori*, but often results in a very high-dimensional function dictionary to approximate the data accurately. The kernel variant of this method, KMD [32] helps with dimensionality reduction, but is once again limited by the choice of the kernel function. A major limitation of all the above multi-layer methods is that the feature maps are treated independent of each other and obtained using local criteria, i.e. by direct function evaluation or projection onto a basis space that is optimal with respect to local features. To overcome these limitations there have been efforts to use deep neural networks (DNNs) to identify multilayer convolution maps [33,34,35] that embed the nonlinear dynamical system into a Koopman basis space with linear dynamics [23]. The success reported from the use of such *deep learning-based Koopman observables* as nonlinear convolution operators to build linear Markov models can be attributed to finding the optimal transformation using multilevel convolution by identifying the appropriate combi-

nations among the different layers in the architecture using an efficient algorithm. While the above work focuses on learning the optimal nonlinear convolution or feature map followed by the linear operator, the work in this article explores learning the overall dynamics using a nonlinear Markov model for the given architecture. Contrasting the two, the former enables prediction of nonlinear dynamics via a linear operator by *learning the appropriate map*, the latter *learns a nonlinear model for the dynamics as a whole* for a given multilayer convolution architecture. Both these Markovian approaches leverage multilayer convolution and deep learning in different ways and have broad implications for data-driven modeling.

As a first step in this paper, we build accurate Markov models of complex nonlinear dynamics from limited data using feature maps whose layers are treated as dependent on each other and computed simultaneously by solving a ‘global’ or ‘non-local’ optimization problem such that the overall learning objective is realized. The aim then is to compare and contrast these approaches with ideas the employ local optimization. To this end, we focus on the ability of a narrow class of SVD-based multi-layer convolution Markov models to capture nonlinear dynamics using globally or non-locally optimized features that we term as *globally optimal convolution (GOC) models* as against *locally optimal convolution (LOC)*. A popular example of multilayer GOC Markov models are feed forward neural networks (FFNN), a robust approach for learning the embedded nonlinearity in the dynamics from data. While shallow NN are known to possess universal function approximation properties [36], it usually requires exponentially large number of neurons (features) for accurate prediction. To overcome this, deep neural networks (DNNs) offer a low-dimensional (short) and layered (deep) alternative for high (almost exponential) representational capacity of complex data. This low-dimensional feature space also helps reduce overfitting in a relative sense. The contribution of this paper is to explore feed forward DNN-like globally optimal multilayer convolution (multilayer GOC or MGOC) as an alternative to locally optimal multilayer convolution (multilayer LOC or MLOC) approaches. We focus our assessment on three popular model architectures:

1. a four-level multi-layer LOC or 4-MLOC framework that mimics dynamic mode decomposition (DMD);
2. a six-level multi-layer LOC of 6-MLOC with a nonlinear mapping that mimics extended DMD (EDMD);
3. a six-level multi-layer GOC or 6-MGOC including nonlinear transfer functions that mimic a feed forward neural network (FFNN).

In all of the above models, the convolution maps are carefully chosen so as to minimize variability so that we can focus purely on the effect of the *local versus global optimization* on the learning of the dynamics. Proper orthogonal decomposition (POD) is used as the first layer in all the above architectures so that we can operate in a low-dimensional feature space.

Through this work, we will show that MGOC models are accurate even with very limited input data as compared to MLOC models with both similar and dissimilar architectures for modeling dynamically evolving fluid flows. We will illustrate that the success of the MGOC architectures can be attributed to extending the dimension of the learning parameters and learning them concurrently using nonlinear optimization. This helps improve robustness and accuracy of the resulting predictions over short and long times as long as sufficient quality data is available. From the analysis in the following sections we show that MLOC models also benefit from the above design, but behave similar to two-layer shallow learning architectures requiring high-dimensional intermediate layers with slower convergence to the accurate result. On the other hand, MGOC being a ‘deep learning’ architecture produces more efficient learning. These ideas will be illustrated using different flow case studies including transient dynamical evolution of a cylinder wake towards a limit-cycle attractor and a transient buoyancy-driven mixing layer. The organization of this paper is as follows. In section 2 we present an overview of data-driven Markov models for transient dynamical systems and their connections to Koopman theoretic methods (section 2.1). In section 2.2, we introduce the concept of locally optimal convolution (MLOC) Markov modeling framework and describe the two variants that we consider in this study in subsections 2.2.1 and 2.2.2. In section 2.3 we introduce the feed forward DNN-like globally optimal convolution (MGOC) framework for building Markov models. The numerical examples and discussion of the modeling performance is presented in section 3 and the various outcomes are summarized with discussion in section 4.

2 Data-driven Markov Models for Transient Dynamical Systems

Extraction of high-fidelity Markov models from snapshot (time) data of nonlinear dynamical systems is a major need in science and engineering, where measurement data can be the only available piece of information. It is advantageous to learn the model in a low-dimensional feature space to both simplify the learning process and also improve efficiency. Most Markov models that are generally learned in the feature space, use linear operators/convolutions to take advantage of the powerful linear systems machinery for control [4], optimization and spectral analysis [10]. A Markov model, for given a current state \mathbf{x}_t and future state \mathbf{x}_{t+T} can be stated as $\mathbf{g}(\mathbf{x}_{t+T}) = \mathcal{K}\mathbf{h}(\mathbf{x}_t)$ where \mathbf{g} and \mathbf{h} are typically finite-dimensional

transformations to the feature space and \mathcal{K} represents the transition operator that can be linear or nonlinear. Without loss of generality, here we will use first order Markov process approximation of the dynamical system. That said, the algorithms presented here can easily be generalized to n^{th} order processes such as $\mathbf{g}(\mathbf{x}_{t+T}) = \mathcal{K}\mathbf{h}(\mathbf{x}_t, \mathbf{x}_{t-T}, \mathbf{x}_{t-2T}, \mathbf{x}_{t-3T} \dots \mathbf{x}_{t-(n-1)T})$. In section 2.1 we explore the connections between the popular Koopman approximation-based methods and Markov linear models. Subsequently, in section 2.2, we introduce a class of locally optimal convolution (MLOC) based Markov models and draw similarities to existing popular models like DMD and EDMD. Finally, in section 2.3 we introduce the globally optimal convolution (MGOC) Markov models.

2.1 Koopman as Markov Linear Model

Linear, first order Markov models can be represented through the class of Koopman operator-theoretic methods [23, 24] as a framework for modeling nonlinear dynamics. In fact, a Markov process can approximate the Koopman operator [23, 24, 10] under certain conditions, namely, $\mathbf{g} = \mathbf{h}$ and \mathcal{K} is linear. This representation is exact when \mathbf{g}, \mathbf{h} and \mathcal{K} are infinite-dimensional. Given a discrete-time dynamical fluid system that evolves as below:

$$\mathbf{y} = \mathbf{x}_{t+T} = \mathbf{F}(\mathbf{x}_t) = \mathbf{F}(\mathbf{x}) \quad (1)$$

where $\mathbf{x}, \mathbf{y} \in \mathcal{M}$ are N -dimensional state vectors, e.g., velocity components at discrete locations in a flow field at a current instant t , and separated by an appropriate unit of time T . To be precise, $\mathbf{x} \triangleq \mathbf{x}_t$ and $\mathbf{y} \triangleq \mathbf{x}_{t+T}$. Operator \mathbf{F} evolves the dynamical system nonlinearly from \mathbf{x} to \mathbf{y} , i.e. $\mathbf{F} : \mathcal{M} \rightarrow \mathcal{M}$. This representation can easily be made relevant to continuous time systems as well as in the limit $T \rightarrow 0$. A general linear Markov description of such a dynamical system is:

$$\mathbf{g}(\mathbf{y}) = \mathbf{g}(\mathbf{x}_{t+T}) = \mathcal{K}\mathbf{h}(\mathbf{x}). \quad (2)$$

Here, $\mathbf{g}(\mathbf{y})$ and $\mathbf{h}(\mathbf{y})$ are vector-valued transformations (components of \mathbf{g}, \mathbf{h} are scalar-valued) to a feature space. In general, $\mathbf{g}, \mathbf{h} \in \mathcal{F}$ (where \mathcal{F} is a function space) are infinite-dimensional, but approximated into a finite-dimensional vector in practice. Consequently, the linear transition operator \mathcal{K} is also a finite-dimensional approximation. In the Koopman framework, the feature space is the observable space and the feature maps are observable functions. The operator theoretic view interprets \mathcal{K} as operating on the observable space [13] $\mathcal{K} : \mathcal{F} \rightarrow \mathcal{F}$. When \mathbf{g} and \mathbf{h} are identical, then the linear operator \mathcal{K} evolves the Markovian dynamics in Eq. (2) as a Koopman evolutionary model given by:

$$\mathcal{K}\mathbf{g}(\mathbf{x}) = \mathbf{g}(\mathbf{y}) = \mathbf{g}(\mathbf{F}(\mathbf{x})). \quad (3)$$

Since, the Koopman operator has the effect of operating on the functions of state space as shown in Eq. (3), it is commonly referred to as a composition operator where \circ represents the composition between \mathbf{g} and \mathbf{F} .

$$\mathcal{K}\mathbf{g} = \mathbf{g} \circ \mathbf{F}. \quad (4)$$

Being a linear operator, the products of Koopman spectral analysis such as the eigenfunctions (ϕ_j), eigenmodes (\mathbf{v}_j) and eigenvalues (μ_j) can be leveraged to reconstruct the transformation $\mathbf{g}(\mathbf{x})$ as shown in Eqs. (5)-(6). This suggests that the transformation \mathbf{g} should be spanned by Koopman eigenfunctions ϕ .

$$\mathbf{g}(\mathbf{x}) = \sum_{j=1}^{\infty} \phi_j \mathbf{v}_j \quad (5)$$

$$\mathbf{g}(\mathbf{y}) = \mathcal{K}\mathbf{g}(\mathbf{x}) = \sum_{j=1}^{\infty} \phi_j \mathbf{v}_j \mu_j \quad (6)$$

In this discussion, we consider sequential snapshots of data separated by a constant time-step and denoted by $(\mathbf{x}^i, \mathbf{x}^{i+1} \dots)$ such that the dynamical system is given by:

$$\mathbf{x}^{i+1} = \mathbf{F}(\mathbf{x}^i) \quad (7)$$

The corresponding Koopman representation is:

$$\mathbf{g}(\mathbf{x}^{i+1}) = \mathbf{g}(\mathbf{F}(\mathbf{x}^i)) = \mathcal{K}\mathbf{g}(\mathbf{x}^i) \quad (8)$$

where, \mathbf{g} is some convolution operator yet to be identified (or assumed for a given model). We can split this sequence of snapshots into pairs as $X = (\mathbf{x}^1 \dots \mathbf{x}^{M-2}, \mathbf{x}^{M-1})$ and $Y = (\mathbf{x}^2 \dots \mathbf{x}^{M-1}, \mathbf{x}^M)$ such that $(X, Y) \in \mathbb{R}^{N \times M}$, then the dynamical system in Eq. (7) can be represented as

$$Y = \mathbf{F}(X) \quad (9)$$

and its quasi-linear form is

$$Y \approx \mathbf{A}(X)X. \quad (10)$$

Here, $\mathbf{A}(X) \in \mathbb{R}^{N \times N}$ is the quasi-linear operator describing the evolution of the discrete dynamical system that we are trying to approximate from data. Where N, M represent the dimensions of the instantaneous system state and the number of available snapshots respectively. Typically, $N \gg M$ and for a nonlinear system $\mathbf{A}(X)$ evolves with X . The observable function \mathbf{g} is usually unknown and approximated with a finite-dimensional convolution map C that can have a functional or data-driven form. We define a convolution operation as a projection of the input state onto an appropriate basis such that the dynamics evolves in a feature space that is often low-dimensional. This would require \mathbf{x}^i be spanned accurately by the choice of basis used to construct the columns of C . To build a finite-dimensional \mathcal{K} in Eq. (8) we define a finite-dimensional convolution $C \in \mathbb{R}^{N \times K}$ such that $\mathbf{g}(\mathbf{x}^i) \approx C\mathbf{x}^i$ and generalized as:

$$X = C\bar{X}, \quad (11)$$

$$Y = C\bar{Y}, \quad (12)$$

where $\bar{X} \in \mathbb{R}^{K \times M}$ and $\bar{Y} \in \mathbb{R}^{K \times M}$ are the corresponding features for X and Y in the feature space, and K is the feature dimension. Note that C is truly nonlinear and should evolve with X as $C(X)$. Eq. (10) can be rewritten as:

$$\mathbf{A}(X)C\bar{X} = C\bar{Y}. \quad (13)$$

Rearranging Eq. (13) gives the relationship below with C^+ , where $(\cdot)^+$ is the Moore-Penrose pseudo-inverse

$$C^+ \mathbf{A}(X)C\bar{X} = \bar{Y}. \quad (14)$$

Defining $\Theta \triangleq C^+ \mathbf{A}(X)C$ as the linear finite-dimensional Koopman operator in the feature space we get:

$$\Theta\bar{X} = \bar{Y}. \quad (15)$$

The fidelity of the above approximation to the dynamical system in Eq. (7) depends on the choice of C as an approximation to observable \mathbf{g} . For Θ to be truly linear, C will have to evolve with the state X as $C(X)$ and $C^+(X)$ needs to exist. For detailed discussion on the architecture and choice of convolution maps we refer to Lu and Jayaraman [14]. Given C, X and Y , we can learn Θ by minimizing the frobenius norm of $\|\bar{Y} - \Theta\bar{X}\|_F$ via $\Theta = \bar{Y}\bar{X}^+$. In principle one could minimize the 2-norm $\|\bar{Y} - \Theta\bar{X}\|_2$ at the risk of added complexity, but the Frobenius norm serves an efficient alternative.

2.2 Markov Model using Multilayer Locally Optimal Convolution (MLOC)

The basis vector onto which the convolution projects the input state needs to be a function acting on the instantaneous state i.e., C should be $C(X)$ so that Θ can be linear. However, this often leads to a futile search for ‘magic’ functions when the nature of $\mathbf{A}(X)$ is not known. Alternative approaches [13, 32] include approximating the functional form of the convolution map from data using a dictionary of basis functions. However, the dependence of C on the choice of functions populating the dictionary and the relative ease with which the feature dimension can grow, limits these approaches. Lu and Jayaraman [14] propose an alternate approach of building complex and efficient convolution maps through layering of elementary operators based on the hypothesis that *deeper and shorter is better than taller and shallow* operators. This is also the key motivation behind the recent boom in *deep learning* ideas for artificial intelligence [37]. It is worth noting that both strategies increase the number of model parameters to be learned, but deep layering offers a sequential way to build model complexity and learn complex patterns much more efficiently than shallow architectures from limited data. A generalized way of building C is to layer recursively multiple convolution operators such as:

$$X = C_1 C_2 \bar{\bar{X}} = \mathcal{C}_{ML} \bar{\bar{X}}, \quad (16)$$

$$Y = C_1 C_2 \bar{\bar{Y}} = \mathcal{C}_{ML} \bar{\bar{Y}}, \quad (17)$$

where $\bar{\bar{X}}$ and $\bar{\bar{Y}}$ represent the features at the 2nd layer and \mathcal{C}_{ML} represents the multilayer convolution operator, a schematic of such process is presented in Fig.1. Where a state vector X is operated by two convolution operators C_1^+, C_2^+ respectively to yield $\bar{\bar{X}}$. Similarly, C_1^+, C_2^+ operate on $Y, \bar{\bar{Y}}$ respectively to yield $\bar{\bar{Y}}$. An approximate linear Koopman operator Θ is then learned using $\bar{\bar{X}}$ and $\bar{\bar{Y}}$. Substituting Eq. (16) and (17) into Eq.(10), we have:

$$AC_{ML} \bar{\bar{X}} = \mathcal{C}_{ML} \bar{\bar{Y}}. \quad (18)$$

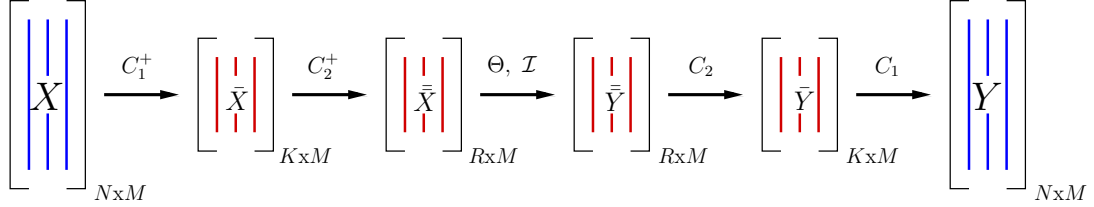


Fig. 1: Schematic of a six-layer representation of the multilayer locally optimal convolution (MLOC) framework to approximate the Koopman operator. X , Y represent state space matrices and C_i^+ , C_i , represent the convolution and reconstruction operations respectively. The arrows indicate direction of the convolution, i.e., C_1^+ acts on X to yield \bar{X} and C_1 acts on \bar{Y} to yield Y . Θ represents an approximate Koopman operator shown in Eq.(8). The size of data matrices in the high (X) and low dimensional (\bar{X} or $\bar{\bar{X}}$) space is also shown.

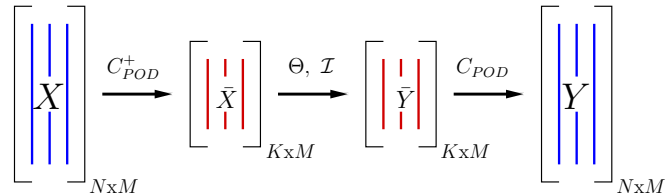


Fig. 2: A four-level Koopman approximation LOC framework with linear maps.

Pre-multiplying the pseudoinverse of \mathcal{C}_{ML} , we have:

$$\mathcal{C}_{ML}^+ A \mathcal{C}_{ML} \bar{X} = \Theta \bar{X} = \bar{Y}, \quad (19)$$

with Θ defined as:

$$\Theta = \mathcal{C}_{ML}^+ A \mathcal{C}_{ML}. \quad (20)$$

In Eq.(20) the convolution can be generalized and consolidated into an effective map given by $\mathcal{C}_{ML}^+ = C_L^+ \dots C_1^+ C_2^+ C_3^+$ and $\mathcal{C}_{ML} = C_3 C_2 C_1 \dots C_L$ to include sufficient number of elementary operators such that an optimal Θ is realized. L represents the number of layers in the design. The forward map or encoder \mathcal{C}_{ML}^+ can be computed as long as the elemental convolution maps, C_i , are invertible in a generalized sense. We note that although the multilayer formulation above is built from a Koopman approximation point of view, i.e. $\mathbf{g} = \mathbf{h} = \mathcal{C}_{ML}$, one can have a generalized Markov version of this model i.e. $\mathbf{g} = \mathcal{C}_{ML1}$ & $\mathbf{h} = \mathcal{C}_{ML2}$. Further, C_i and consequently \mathcal{C}_{ML} are usually predetermined convolution maps (or functions) or computed using only the locally available information. Hence, we call this class of methods as *locally optimal convolution* or LOC for short. In the following subsections 2.2.1 and 2.2.2 we will view the popular Koopman approximation methods in the context LOC class of methods.

2.2.1 A Four-level Multilayer Locally Optimal Convolution (4-MLOC) Map

There exist many methods to approximate the Koopman tuples including DMD [11,12], EDMD [13] and its kernel variants [32] and generalized Laplace analysis (GLA) [23]. DMD [12] employs a linear identity map between the observable and input state spaces and hence, also represents a linear model in the original input space. The architecture for DMD is shown in Fig.2 as a four-level architecture (4-MLOC) with a single POD convolution map obtained via SVD [16] from snapshots of data (X). Given data snapshots separated in time X, Y as before, we can apply the convolution operator as:

$$X = C_{POD} \bar{X}; \quad Y = C_{POD} \bar{Y}. \quad (21)$$

Substituting the above in Eq. (19), we get the linear model below

$$\Theta \bar{X} = \bar{Y} \quad (22)$$

where \bar{X} and \bar{Y} are snapshots of POD coefficients evolving in time and represent the dynamics of the nonlinear fluid flow in the feature space. Θ is a finite dimensional approximation of the Koopman operator,

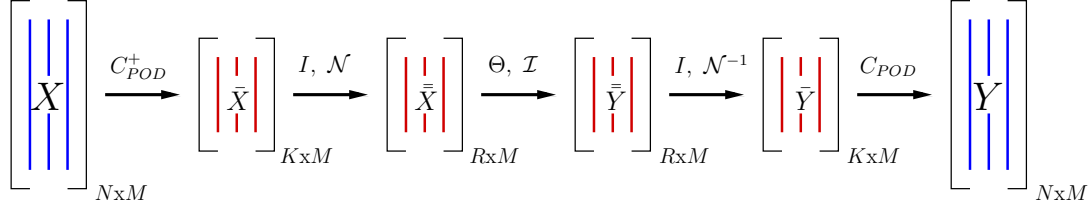


Fig. 3: A six-level Koopman approximation LOC framework with nonlinear maps (\mathcal{N} , \mathcal{N}^{-1}) with I representing identity convolution operation.

a linear transition operator governing the dynamics of the flow in the feature space. The pairs \bar{X} and \bar{Y} are setup as follows:

$$\bar{X} = \begin{bmatrix} a_1^1 & a_1^2 & \dots & a_1^{M-1} & a_1^M \\ a_2^1 & a_2^2 & \dots & a_2^{M-1} & a_2^M \\ \cdot & \cdot & \dots & \cdot & \cdot \\ \cdot & \cdot & \dots & \cdot & \cdot \\ a_K^1 & a_K^2 & \dots & a_K^{M-1} & a_K^M \end{bmatrix}_{(K \times M)} \quad \text{and} \quad \bar{Y} = \begin{bmatrix} a_1^2 & a_1^3 & \dots & a_1^M & a_1^{M+1} \\ a_2^2 & a_2^3 & \dots & a_2^M & a_2^{M+1} \\ \cdot & \cdot & \dots & \cdot & \cdot \\ \cdot & \cdot & \dots & \cdot & \cdot \\ a_K^2 & a_K^3 & \dots & a_K^M & a_K^{M+1} \end{bmatrix}_{(K \times M)}. \quad (23)$$

Knowing Θ allows one to model the evolution of this dynamical system through the weights. Within the context of a multilayer framework, DMD can be viewed as a 4-level set-up (or 2-layer without the POD-convolution) with the first and last layers mapping in and out of the POD feature space respectively. Given that the convolution operator C_{POD} is independent of X , we can treat this model as a local optimization between the two layers in the middle as seen in Fig.2. This local optimization problem tries to find an optimal mapping between all pairs of features $\mathbf{a}^t, \mathbf{a}^{t+1}$ which are column vectors in \bar{X}, \bar{Y} as shown below,

$$\bar{Y} = [\mathbf{a}^2 \mathbf{a}^3 \dots \mathbf{a}^{t+1} \dots \mathbf{a}^{M+1}] = \Theta [\mathbf{a}^1 \mathbf{a}^2 \dots \mathbf{a}^t \dots \mathbf{a}^M] = \Theta \bar{X} \quad (24)$$

such that $(\bar{Y} - \Theta \bar{X})$ [16] is minimized. While there exists many approaches to solving this optimization problem, we minimize the Frobenius norm of $\|\bar{Y} - \Theta \bar{X}\|_F$ via,

$$\Theta = \bar{Y} (\bar{X} + \lambda I)^+ \quad (25)$$

where $(\cdot)^+$ denotes the generalized Moore-Penrose pseudo-inverse [16] and λ is regularization [38] parameter used to generate a unique solution from the pseudo-inverse and also avoid overfitting. In this 4-layer architecture, the convolution maps between any two layers are treated independently, i.e. C_{POD} does not depend on Θ which also implies that minimization of $\|\bar{Y} - \Theta \bar{X}\|_F$ is not the same as minimizing $\|Y - AX\|_F$. The equivalence between these two minimization problems depend on the choice of the convolution C .

2.2.2 A Six-level Multilayer Locally Optimal Convolution (6-MLOC) Map

Dynamic mode decomposition (DMD) being a linear model with a fixed POD features has difficulties predicting transient nonlinear fluid flows [11, 14]. Extensions to DMD such as EDMD [13, 11] help alleviate this problem to some extent by introducing nonlinear convolution layer(s) as a wrapper to the POD-layer in DMD. It can also be viewed as combining POD convolution with a transfer function (TF) that creates an extended polynomial basis up to a desired order. In this way, it is a multilayer convolution framework with nonlinear transfer functions as shown Fig.3. This architecture can be viewed as a 6-level framework (4-layer without the POD-convolution) or 6-MLOC with the first and fifth pair of layers representing a POD-convolution while the 2nd and 4th pair of layers representing the nonlinear feature maps. Because, the architecture represented in Fig.3 has a ‘forward’ depiction, the nonlinear mapping in the 4th layer is denoted with an inverse function \mathcal{N}^{-1} . It is worth noting that in practice, \mathcal{N}^{-1} may not be well behaved and hence the backward operation is preferred. This is another way of representing Koopman approximation methods which are intrinsically forward-backward maps. The linear Koopman operator is then approximated through a least squares minimization problem, $\|\bar{Y} - \Theta \bar{X}\|_F$ solved in a similar way as Eqn.(25).

In this study, we present two variants of this method, namely 6-MLOC-P (EDMD-P) [13] which uses polynomial basis dictionary for incorporating nonlinearity into the convolution map and 6-MLOC-TS

(EDMD-TS) which uses tansigmoid as a nonlinear feature map. An illustrative representation of the 6-MLOC-P (EDMD-P) with 2nd order polynomial is presented in Fig.5(a), where \mathbf{a} and $\bar{\mathbf{a}}$ represent the columns of \bar{X} , $\bar{\bar{X}}$ and are related as

$$\bar{\mathbf{a}}^i = \mathcal{N}(\mathbf{a}^i) \quad (26)$$

Here \mathcal{N} is the nonlinear operator representing both polynomial generation for 6-MLOC-P (2nd order or higher) and tansigmoid function evaluation for 6-MLOC-TS (EDMD-TS) as the choice may be. A mathematical representation of polynomial with $P = 2$ and tansigmoid operators are presented in Eqns.(27) & (28),

$$\bar{\mathbf{a}} = \mathcal{N}(\mathbf{a}) = \begin{bmatrix} \mathbf{a} \\ \mathbf{a} \otimes \mathbf{a} \end{bmatrix} \quad (27)$$

$$\bar{\mathbf{a}} = \mathcal{N}(\mathbf{a}) = \tanh \mathbf{a} \quad (28)$$

where $\bar{\mathbf{a}}$ represent the features in the \mathcal{N} space. It can be easily seen from above that MLOC-P (EDMD-P) leads to a quadratic growth in the dimension of the features for 2nd order nonlinearity. This will be even worse for higher order polynomial basis. On the other hand, MLOC-TS (EDMD-TS) does not lead to increase in the number of features. A key aspect of both the DMD and EDMD-type architectures is that the different convolution operators (layers) are independent of each other, i.e. C_{POD} , \mathcal{N} and Θ do not depend on each other and hence classified as ‘local’ operators. As a consequence of this layer-wise independence, we can perform both backward and forward convolutions which allows for learning the Koopman operator and allows one to solve for Θ directly (non-iteratively). In the following section, we will focus on globally optimal convolution (GOC) operators with dependent convolutions that forces one to solve for Θ collectively (globally).

2.3 Markov Model Using Multilayer Globally Optimal Convolution (MGOC)

In principle, multilayer convolution increases the number of hyperparameters in the model. In the earlier discussion on layer-wise LOC models, we bypassed this additional complexity by learning the convolution map offline (i.e. learning C_{POD} from training data) or assumed a functional form of the convolution (\mathcal{N}). To constrain the model to the data, we still had to solve the local optimization problem via Eq.(25) within a single-layer. While this approach makes MLOC methods efficient but they do not take advantage of the extended hyperparameter space for learning the system. Consequently, such methods work only for predicting select dynamics and fails to capture highly nonlinear transient dynamical systems. To truly take advantage of the extended hyperparameter space offered by the multilayer convolution framework, the convolution maps relating each layer need to be optimized for improved learning and prediction. Further, this optimization needs to be performed in a coordinated fashion so that a global objective can be minimized. This framework can be interpreted as a *multilayer globally optimal convolution (MGOC)* based Markov model. It turns out that the MGOC architectures are like neural networks which allows us to leverage the various algorithmic advancements [30]. In this study we present a MGOC architecture inspired from feedforward neural networks (FFNN) as shown in 4. Fig. 5(b) presents this architecture as is commonly observed in the machine learning except for the absence of a bias term. We deliberately removed the bias term in order to facilitate better comparison with conventional MLOC architectures such as DMD and EDMD.

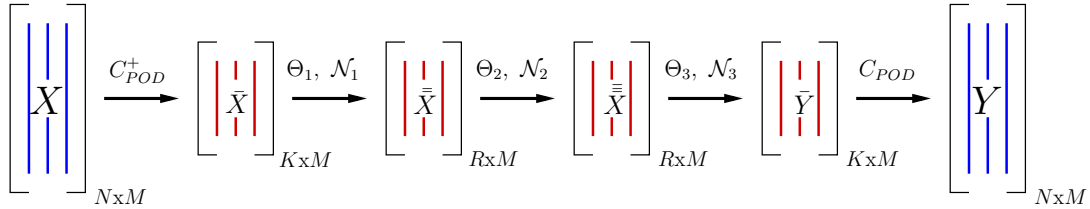


Fig. 4: A six-level Multi layer GOC (6-MGOC) framework inspired from feed forward neural network architectures in machine learning and artificial intelligence, where Θ_l , \mathcal{N}_l with arrow represents a convolution operation followed by a nonlinear mapping (see Eq.(32)) respectively.

We chose a 6-layer architecture to compare with the 6-MLOC in section 2.2.2 so that a fair assessment of the different models can be made. Further, we retain the POD-based map as the first and last convolution operators so that the feature dimensions remain manageable for the fluid flow examples considered in this study. Each interior convolution map includes a linear map Θ_l and a nonlinear transfer function \mathcal{N}_l that is predetermined for each version of the model. To mimic the 6-MLOC model exactly, one will need to set $\Theta_1 = \Theta_3 = I$, the identity tensor & $\mathcal{N}_1 = \mathcal{N}$, $\mathcal{N}_3 = \mathcal{N}^{-1}$ along with $\Theta_2 = \Theta$ & $\mathcal{N}_2 = \mathcal{I}$ as an identity map. For this FFNN-like MGOC architecture that only supports forward maps, building a convolution map with \mathcal{N}^{-1} is not explored currently. This is because, for many common choices of \mathcal{N} , \mathcal{N}^{-1} is not always bounded. It is for this reason, even in the MLOC architectures, the backward operation is preferred. However, in general the various Θ_l are computed simultaneously by solving a coupled optimization problem. As before, \bar{X}, \bar{Y} represent the time snapshots of POD weights of the data separated by the same unit of time as shown in Eq. (24) with columns made of \mathbf{a}^t and \mathbf{a}^{t+1} respectively. In this case, we predict \bar{Y} using \bar{X} as shown below:

$$\bar{\bar{X}} = \mathcal{N}_1(\Theta_1 \bar{X}), \quad (29)$$

$$\bar{\bar{X}} = \mathcal{N}_2(\Theta_2 \bar{\bar{X}}), \quad (30)$$

$$\bar{Y}_p = \mathcal{N}_3(\Theta_3 \bar{\bar{X}}). \quad (31)$$

In general, we have for a general multilayer network

$$X_l = \mathcal{N}_l(\Theta_l X_{l-1}). \quad (32)$$

where \bar{Y}_p is the predicted data and $X_l, \Theta_l, \mathcal{N}_l$ represents the mapped features, linear operator and nonlinear map relating the l^{th} and $l+1^{th}$ layers. The linear operator Θ_l , with $l = 1 \dots (L-3)$, for a L -layer framework is computed by minimizing the overall cost function defined as:

$$\mathcal{J}(\Theta) = \underbrace{\frac{1}{2M} \sum_{i=1}^N \sum_{j=1}^M (\bar{Y}_p(j, i) - \bar{Y}(j, i))^2}_{\text{Feed forward Cost}} + \underbrace{\left(\frac{\lambda}{2M} \sum_{l=1}^{L-3} \sum_{s=1}^S \sum_{q=1}^Q (\Theta_l(s, q))^2 \right)}_{\text{Regularization term}} \quad (33)$$

where \bar{Y} is the original data, S, Q represent the dimension of the features in layers l and $l+1$ respectively. In this architecture, we number the layers of features, l from $0 \dots L-2$. For example, in the 6-MGOC network shown in fig. 4 we have $L = 6$ including the first ($l = 0$) and last ($l = 5$) POD convolution and deconvolution layers. This architecture will consist of Θ_l , l from $0 \dots 4$ with $\Theta_0 = C_{POD}^+$ and $\Theta_4 = C_{POD}$ while Θ_1, Θ_2 and Θ_3 are computed simultaneously. The optimal solution for Θ_l is obtained using back-propagation algorithm with a gradient descent framework employing a Polack-Ribiere conjugate gradient algorithm [39] that employs a Wolfe-Powell stopping criteria. The use of back propagation to find Θ 's is the most important distinction between MLOC and MGOC methods. This gradient descent framework requires \mathcal{N}_l to be infinitely differentiable which is not always guaranteed when choosing $\mathcal{N}_l = \mathcal{N}^{-1}$. Consequently, we choose the nonlinear functions \mathcal{N}_l in 6-MGOC as $\mathcal{N}_{1,2} = \mathcal{N}$ and $\mathcal{N}_{3,4} = \mathcal{I}$. To avoid overfitting in Eq.(33), we use \mathcal{L}_2 norm based regularization while computing Θ 's, with λ as the tuning parameter similar to that used in the MLOC architectures. In the case of learning linear operators, this l_2 penalty boils down to the well known Tikhonov regularization. For assessment purposes, we use two intermediate layers in the MGOC (when learning the dynamics between \bar{X} and \bar{Y}) as illustrated in figure 5 to resemble the construct of 6-MLOC (EDMD). Standard FFNN employs a bias term in Eq.(29), but is not considered here for this comparison study. To determine the dimension of the intermediate layer features in MGOC we use a factor (N_f) that is multiplied with the input feature dimension, i.e., $S, Q = N_f \times$ input feature dimension. The key distinction between MLOC and the FFNN-like MGOC is the lack of a forward-backward mapping in the latter which does not support the learning of the Koopman operator. To accomplish this, the MGOC framework (FFNN) needs to be modified with feedback loops that have similarities to RNNs. Such a modified architecture is presented in [33].

3 Numerical Experiments and Discussion

In this section we compare the predictive capabilities of MLOC framework that uses local optimization with FFNN-like MGOC frameworks based on global optimization. Our hypothesis is that learning an extended hyperparameter space by minimizing the training error-based cost function allows for improved predictions of time-series flow data. Consistent with the earlier sections, we adopt the nomenclature ‘L-Method- $\mathcal{N}M$ ’ to denote the different architectures and their respective parameters, where the ‘L’ represents the total number

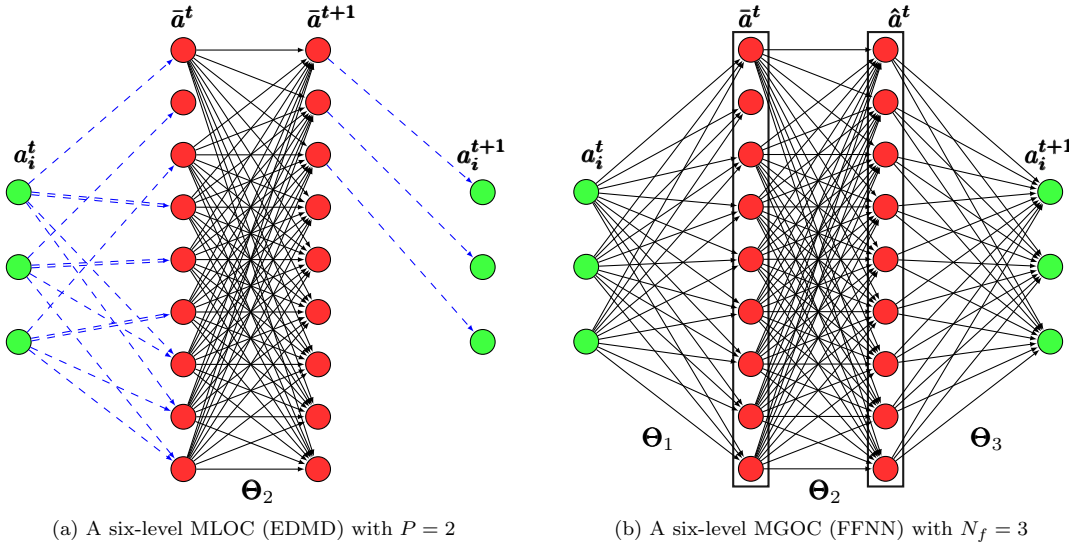


Fig. 5: A representative comparison of architectures (a) 6-MLOC (EDMD-P) and (b) 6-MGOC (FFNN) methods which use local and non-local optimization, respectively

of layers used to map from state space to state space ($X \rightarrow Y$), \mathcal{N} defines the intermediate (nonlinear) convolution and M represents any specific parameters that supplement \mathcal{N} . For example, we describe a 6-level multilayer-locally optimal convolution (EDMD) with a polynomial convolution of 2^{nd} order as 6-MLOC-P2, while a 6-level MLOC (EDMD) with a tansigmoid function is described as 6-MLOC-TS1 where the number followed by TS represents the feature growth factor (N_f). A 4-level MLOC representing the DMD architecture is denoted as 4-MLOC- $\mathcal{I}1$, where \mathcal{I} defines identity mapping and $M = 1$ defines the feature growth factor. In this study, we have used four MGOC architectures with different feature growth factors so as to compare and assess the abilities of the GOC framework over their LOC counterparts. The MGOC methods used are 6-MGOC-TS with $N_f = 1, 3, 9, 20$. The various model possibilities are delineated in section 3.2. Section 3.1 details the generation of flow data from high fidelity computations for use in this study, namely the cylinder wake flow (sec. 3.1.1) and the buoyancy-driven mixing flow (sec. 3.1.2).

3.1 Data generation

To assess the different modeling architectures and the learning algorithms, we build a database of snapshots of transient flow field data generated from high fidelity CFD simulations of a bluff body wake flow and also buoyancy-driven mixing layer. Both these flows are transient in their own way. The cylinder wake flow evolves on a stable attractor and approaches limit-cycle behavior rather quickly while the buoyancy-driven flow is a transient mixing problem with dynamics that dies out in the long-time limit. The former is an example of data-rich situation where the training data requirement to predict the dynamics is limited. On the other hand, the latter represents a data-sparse situation where the training data may not be sufficient to predict the future evolution. We explore the performance of the MLOC and MGOC architectures for both these situations with different combinations of training and prediction regimes. In the following section, we detail the data generation process for both these flows.

3.1.1 Transient Wake Flow of a Cylinder

Studies of cylinder wakes [40, 41, 19, 11] have attracted considerable interest from the flow system learning community for its particularly rich flow physics content, encompassing many of the complexities of nonlinear dynamical systems, while easy to simulate accurately on the computer using established CFD tools. In this exploration into the performance of different data-driven modeling frameworks we leverage both the unstable transient (evolution towards a limit cycle) and the stable limit-cycle dynamics of two-dimensional cylinder wake flow at two Reynolds numbers, $Re = 100, 1000$. To generate two-dimensional cylinder flow data, we adopt the spectral Galerkin method [42] to solve incompressible Naiver-Stokes equations, as shown in Eq. (34) below:

$$\frac{\partial u}{\partial x} + \frac{\partial u}{\partial y} = 0, \quad (34a)$$

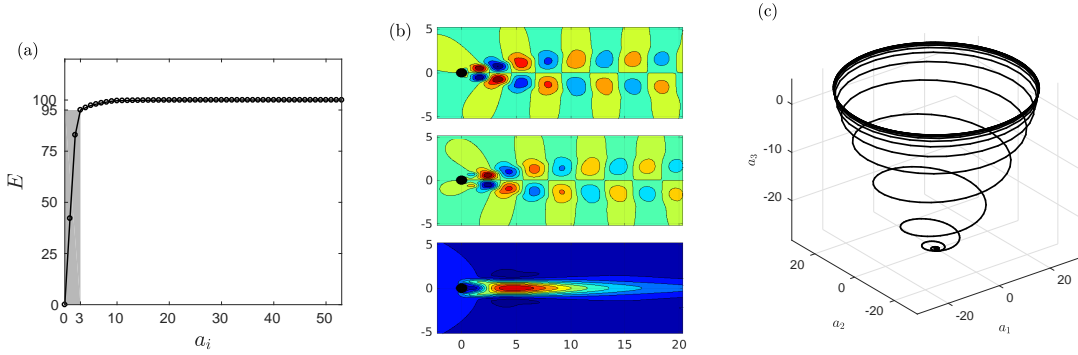


Fig. 6: Energy content in POD features (a) 3 coefficients (b) eigen modes/functions corresponding to 3 POD features (c) phase portrait of $Re = 100$ flow.

$$\frac{\partial u}{\partial t} + u \frac{\partial u}{\partial x} + v \frac{\partial u}{\partial y} = -\frac{\partial P}{\partial x} + \nu \nabla^2 u, \quad (34b)$$

$$\frac{\partial v}{\partial t} + u \frac{\partial v}{\partial x} + v \frac{\partial v}{\partial y} = -\frac{\partial P}{\partial y} + \nu \nabla^2 v, \quad (34c)$$

where u and v are horizontal and vertical velocity components. P is the pressure field, and ν is the fluid viscosity. The rectangular domain used for this flow problem is $-25D < x < 45D$ and $-20D < y < 20D$, where D is the diameter of the cylinder. For the purposes of this study, a reduced domain, i.e., $-2D < x < 10D$ and $-3D < y < 3D$, is used. The mesh was designed to sufficiently resolve the thin shear layers near the surface of the cylinder and transit wake physics downstream. For the case of $Re = 100$ the grid includes 24,000 points whereas for $Re = 1000$ the grid is refined to include approximately 95,000 points for the sampled flow region. The computational method employed is fourth order spectral expansions within each element in each direction. Each data snapshot output was sampled at $\Delta t = 0.2$ non-dimensional time units. With the velocity data arranged as described in section 2.1, a SVD of state vectors was performed to obtain POD coefficients and their respective modes. The most dominant POD coefficients corresponds to eigenvalues at $St = 0.16$ and 0.23 for $Re = 100$ and 1000 , from which we have deduced the number of data points that encompass one limit cycle. Each limit cycle contains approximately 31 and 21 data points of POD coefficients. In this study we have used the convention of cycles to specify the training region, so as to provide a better physical representation to the training data used, while this also helps in making observations on long time predictions (cycles) based on limited number of data(cycles) provided.

Although, a minimum > 15 POD modes are required for nearly 100% energy reconstruction of cylinder flows at $Re = 100$ and 1000 , the large scale coherent structures which govern the flow dynamics are represented by the first 3 modes and account for approximately 95% and 90% energy respectively, see Figs.6(a) and 7(a). The eigenfunctions corresponding to these three modes are presented in Figs.6(b) and 7(b) respectively and show qualitatively similar flow structures for both $Re = 100$ and $Re = 1000$. In Figs.6(c) and 7(c) we show the phase portrait for the flow dynamical system, wherein the flow transitions from a steady wake through an instability and settles on a limit cycle attractor.

3.1.2 2D Buoyant Boussinesq Mixing Flow

The previous case represents a nonlinear dynamical system that evolves asymptotically towards a limit-cycle attractor. Such systems can be predicted in the limit of sufficient data [14]. The Boussinesq buoyant mixing flow [43,44] also known as the unsteady lock-exchange problem [45] exhibits strong shear and Kelvin-Helmholtz instability phenomena driven by the temperature gradients. As the Boussinesq flow is highly convective and instability driven, such a system state cannot be represented by a compact set of POD modes. Rather, the low-dimensional manifold itself evolves with time which makes this a highly data-sparse system. Further, any noise in the initial data can produce unexpected deviations that makes such systems hard to model even using equation-driven models such as POD-Galerkin [45]. We know from previous work [14] that such problems are hard to predict well using MLOC framework. yet, we include this data-set as part of our assessment toolkit to determine if MGOC methods can improve predictions for such systems.

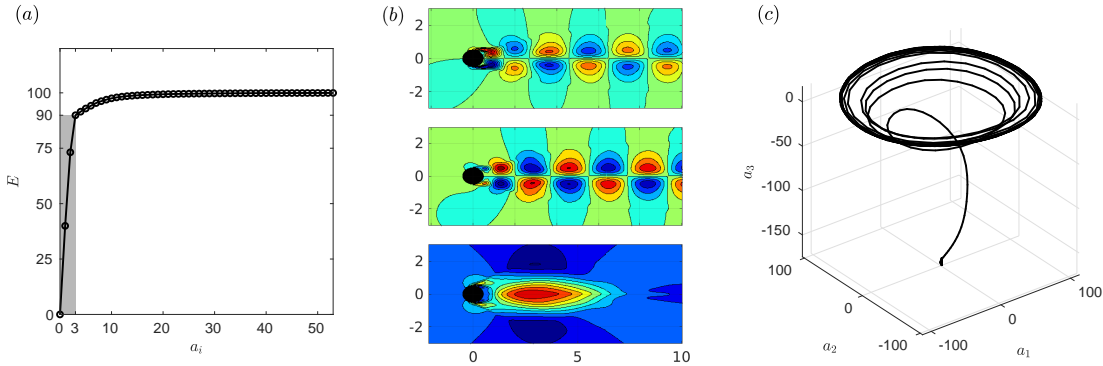


Fig. 7: Energy content in POD features selected (a) 3 coefficients (b) eigen modes/functions corresponding to 3 POD features (c) phase portrait of $Re = 1000$ flow.

The data set is generated by solving the dimensionless form of the two-dimensional incompressible Boussinesq equations[45], as shown in Eq. 35 on a rectangular domain that is $0 < x < 8$ and $0 < y < 1$.

$$\frac{\partial u}{\partial x} + \frac{\partial u}{\partial y} = 0, \quad (35a)$$

$$\frac{\partial u}{\partial t} + u \frac{\partial u}{\partial x} + v \frac{\partial u}{\partial y} = -\frac{\partial P}{\partial x} + \frac{1}{Re} \nabla^2 u, \quad (35b)$$

$$\frac{\partial v}{\partial t} + u \frac{\partial v}{\partial x} + v \frac{\partial v}{\partial y} = -\frac{\partial P}{\partial y} + \frac{1}{Re} \nabla^2 v + Ri\theta, \quad (35c)$$

$$\frac{\partial \theta}{\partial t} + u \frac{\partial \theta}{\partial x} + v \frac{\partial \theta}{\partial y} = \frac{1}{RePr} \nabla^2 \theta, \quad (35d)$$

where u , v , and θ are the horizontal, vertical velocity, and temperature components, respectively. The dimensionless parameters Re , Ri , and Pr are the Reynolds number, Richardson number, and Prandtl number, respectively with values chosen as follows: $Re = 1000$, $Ri = 4.0$, and $Pr = 1.0$. This physics is modeled on a 256×33 grid. Initially fluids at two different temperatures are separated by a vertical line at $x = 4$. The bounding walls are adiabatic and have friction. To obtain an accurate data representation, a fourth-order compact finite difference scheme is used to compute the derivatives in Eq. 35. The evolution of the thermal field over the simulation time range of 32 seconds is shown in fig. 8 and illustrates the highly transient nature of the dynamics. To reduce the dimensionality of the system state POD modes computed from the entire data set with 1600 snapshots is employed. The reduced feature set consisting of three POD features (capturing nearly 80% of the total energy) representing a low resolution measurement is shown in fig. 9 is used to train the model and predict the trajectory.

3.2 Analysis Framework

In this section we summarize the different candidate model architectures and the corresponding learning algorithms. Table 1, lists the different MLOC architectures and their corresponding MGOC architectures with the total number of learning parameters (\mathcal{LP}) used. The first sub-column under each local (LOC) and globally (GOC) architecture in table 1 represents the choice of nonlinear part of the convolution map and the second sub-column represents the different layers with the corresponding feature dimension. For readability and conciseness, we have excluded the first and last layers corresponding to the input and output state vectors acted on by a POD-convolution. The rightmost column represents the total number of learning parameters (\mathcal{LP}) in a model. For example, when using 6-MLOC-P2 in table 1 we learn an operator (Θ) with 81(9x9) parameters to model the flow and similarly, using 6-MGOC-TS for TS3 we learn operators($[\Theta_1, \Theta_3, \Theta_3]$) totaling 135(27 + 81 + 27) parameters.

The six-level 6-MLOC-P2 (quadratic polynomial features) method produces 9 features in the intermediate layer which is then used to learn a locally optimal mapping between the 9 features at the next intermediate layer followed by reverse map to the penultimate layer with 3 POD features. A similar construct can be observed in globally optimal framework using 6-MGOC-TS with $N_f = 3$. However, the 6-MLOC-P2 consists of 81 parameters while the 6-MGOC-TS has 135. In our following analysis of the various predictions,

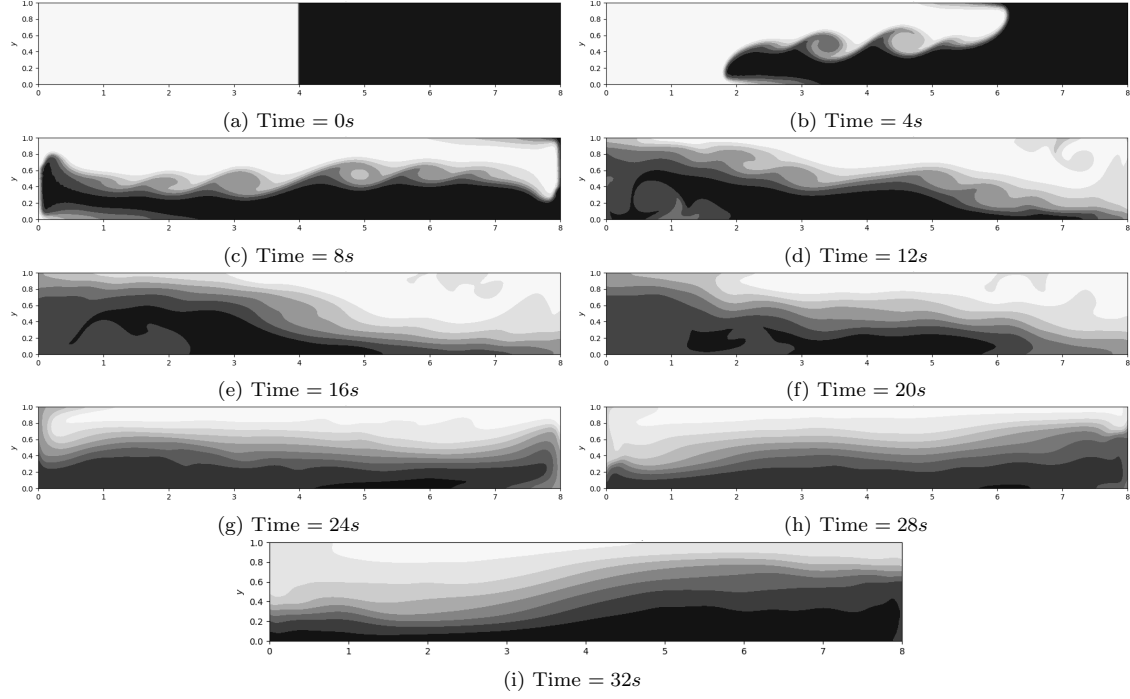


Fig. 8: Time evolution of the temperature field in the buoyant Boussinesq mixing flow is shown over a period of 32 sec of simulation time.

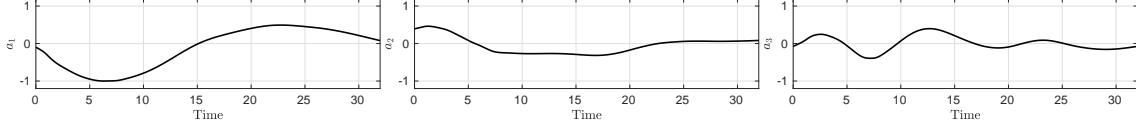


Fig. 9: Time evolution of the POD weights, a_i^t for the buoyant mixing flow.

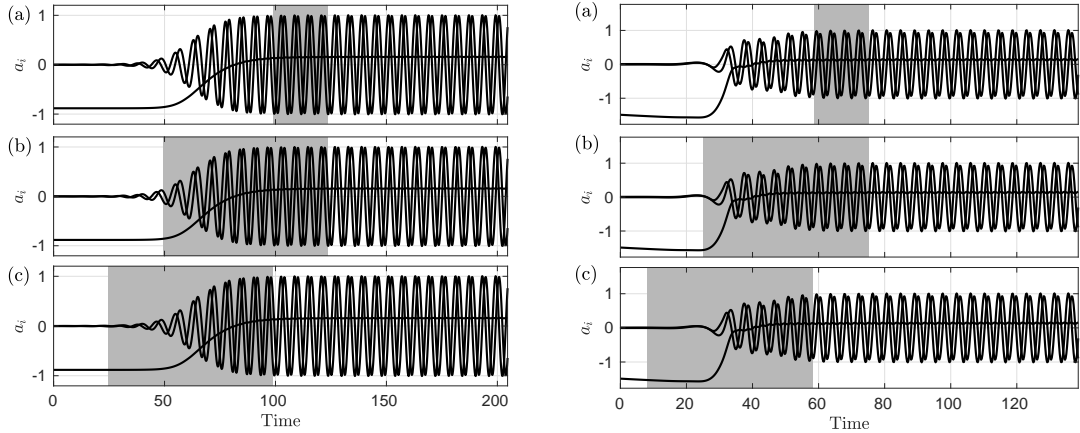
we find that using just 3 POD features with a 2nd order polynomial expansion in 6-MLOC-P2 does not produce accurate results. So, in addition to P2, we also explore higher order polynomial basis to ascertain if better predictions can be realized. In the following subsection, we describe the prediction and analysis methodology.

	Local optimization		\mathcal{LP}	Global optimization		\mathcal{LP}
	4-MLOC- \mathcal{I}	6-MLOC- \mathcal{I}		6-MGOC- \mathcal{I}	6-MGOC-TS	
1	$\mathcal{I}1$	3-3	9	$\mathcal{I}1$	3-3-3-3	27
2	6-MLOC-TS			TS1	3-3-3-3	27
3	6-MLOC-P			TS3	3-9-9-3	135
	P2	3-9-9-3	81	TS9	3-27-27-3	891
	P7	3-125-125-3	15,625	TS20	3-60-60-3	3960

Table 1: Overview of the methods used as part of this analysis. The dimensions of the different layers correspond to that used for cylinder wake flow model.

3.3 Prediction Framework and Error Metrics

The data generated from the computer simulations described above are separated into training and prediction regimes. The training data set is used for learning the optimal Θ 's using which future time predictions



(a) Times series plot of the weights corresponding to the three most energetic POD modes with different training regions (a) most energetic POD modes with different training regions (a) Limit cycle (16 – 20): 124 data points, (b) transient region-I Limit cycle (14 – 18): 84 data points, (b) transient region-I (8 – 20): 372 data points and (c) Transient region-II (4 – 16): (6 – 18): 252 data points and (c) Transient region-I (2 – 14): 372 data points, where each cycle consists of 31 data points. (b) Times series plot of the weights corresponding to the three most energetic POD modes with different training regions (a) most energetic POD modes with different training regions (a) Limit cycle (16 – 20): 124 data points, (b) transient region-I Limit cycle (14 – 18): 84 data points, (b) transient region-I (8 – 20): 372 data points and (c) Transient region-II (4 – 16): (6 – 18): 252 data points and (c) Transient region-I (2 – 14): 372 data points, where each cycle consists of 21 data points.

Fig. 10: Schematic showing the different training regions chosen for prediction using the different models.

are computed with input specified from the previous time step alone to mimic a practical usage of the model. In this study, we assess model performance based on both qualitative representation of the dynamics and prediction errors. We quantify model errors using the \mathcal{L}_2 norm of the prediction error from the data-driven model relative to the truth using only the initial condition \mathbf{a}_0 specified. To bypass the complexities of computing the 2–norm, the Forbenius norm of the error is computed instead as below.

$$\mathcal{E}_i = \frac{1}{2M_i} \|\bar{Y}_p - \bar{Y}\|_2^2. \quad (36)$$

In the above equation \bar{Y}_p represents the data-driven model predictions and \bar{Y} the true data. We separately quantify the errors in the training region where the data-driven model is more of an interpolation and in the prediction region where model performs an extrapolation role. The prediction error in the training region is denoted by \mathcal{E}_t and combined error in both the training and prediction regions is denoted by \mathcal{E}_p . As a way to assess the robustness of the different models discussed in table 1 we explore their ability to predict the flow dynamics given an initial condition in any part of the flow dynamics, for example, in transient or limit cycle regions for the cylinder wake flow. To this end, we designed three training regions (see Fig. 10a) corresponding to three different time windows. In Figs. 10a and 10b we show these three training regions used for data with $Re = 100$ and $Re = 1000$ respectively, shaded in grey. The figures in row (a) represent the training region in the limit-cycle regime and rows (b) and (c) show two regions in the transition part of the dynamics and denoted by region I (TR-I) and region II (TR-II). A challenging test for a model is to learn the dynamics in the steady wake flow as shown in Figs. 10a and 10b and predict the instability growth that ultimately results the limit cycle. In our experience using training data that only contains information of the steady wake produces models that are highly unstable. Consequently, we designed two different training regions where the flow transitions across flow regimes, but with different proportions of limit-cycle (vortex shedding) and steady wake content. In the following sections we will highlight and discuss the key results from our data-driven predictions.

3.4 Learning and Predicting Limit-cycle Cylinder Wake Dynamics

The focus of this section is to learn from limit-cycle training data and predict the corresponding limit-cycle physics over long-times. Successful prediction of this case is considered a benchmark for data-driven models. The underlying theme in this article is to explore whether globally optimal learning of the model parameters (\mathcal{LP}) can outperform locally learnt model parameters for predictions. To verify this we compare the following four models namely: 4-MLOC- $\mathcal{I}1$ (DMD), 6-MGOC- $\mathcal{I}1$ (compares favorably with FFNN-linear), 6-MLOC-TS1 (EDMD-TS1) and 6-MGOC-TS1 (compares favorably with FFNN-TS). It is well known that 4-MLOC- $\mathcal{I}1$ or DMD performs well in the limit cycle region as shown in [14,11] and under performs in the strongly nonlinear transition regimes on account of being a linear model. In Fig.11, the time series predictions of the first three POD features are shown. with rows 1–4 (top-to-bottom) representing the

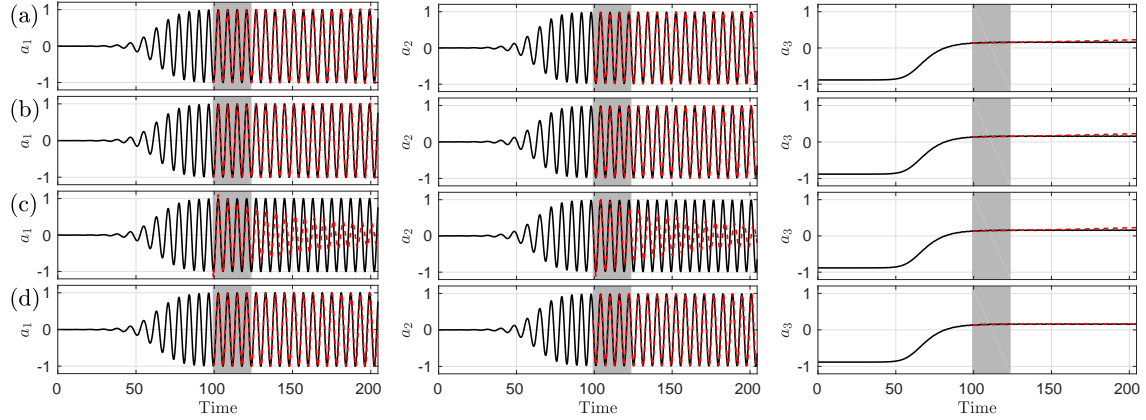


Fig. 11: Times series of predicted POD features (---) obtained from (a) 4-MLOC- $\mathcal{I}1$, (b) 6-MGOC- $\mathcal{I}1$, (c) 6-MLOC-TS1 and (d) 6-MGOC-TS1 are plotted with their respective original data (—) in the limit cycle regime.

prediction outcomes from the learned parameters (Θ) obtained using the 4-MLOC- $\mathcal{I}1$ (DMD), 6-MGOC- $\mathcal{I}1$ (FFNN-linear), 6-MLOC-TS1 (EDMD-TS1) and 6-MGOC-TS1 (FFNN-TS1) architectures respectively. It is worth noting that 4-MLOC- $\mathcal{I}1$ (DMD) and 6-MGOC- $\mathcal{I}1$ are a pair of local and global models with a linear transfer (convolution) function. In the same vein, 6-MLOC-TS1 (EDMD-TS1) and 6-MGOC-TS1 (FFNN-TS1) are a pair of linear and global models with a nonlinear tansigmoid transfer function. Specifically, we assess the role of local(LOC) versus global (GOC) optimization of the parameters as well as the impact of nonlinear mapping on model prediction.

The first major observation is that both the GOC as well as the LOC models with linear mapping predict the overall dynamics relatively accurately while the LOC model with nonlinear sigmoid mapping damps the POD features over time. The second observation is that all the models show gradual error growth with time except the 6-MGOC-TS1 architecture which is closer to a FFNN-TS. The plots in Fig.11 convey that a nonlinear mapping is not essential to capture the limit-cycle dynamics, but if used, should be carefully designed. For example, it was shown in [14] that EDMD-P2 (6-MLOC-P2) can predict such dynamics very well while the current results (Fig.11(c)) show that the same architecture with a tansigmoid function produces errors. The TS function is primarily used in machine learning for classification and has a *squashing* nature to it, i.e. it has the effect of compressing the features which explains its inability to predict the dynamics. This occurs in spite of using \mathcal{N}^{-1} as the ‘reverse squashing’ map in the architecture as discussed in sec. 2.2. A plausible reason could be that the TS nonlinearity does not extend the space of learning parameters in contrast to polynomial basis. Nevertheless, when the TS nonlinearity (using the \mathcal{N}) is combined with a GOC framework such as in 6-MGOC-TS1, the prediction drastically improves as learning the mapping parameters in $\Theta_1, \Theta_2, \Theta_3$ simultaneously while applying the TS nonlinearity produces a compensatory and powerful outcome. Further, this FFNN-like 6-MGOC-TS1 model can predict over long times without growth in error as seen from the evolution of third POD feature (shift mode) in Fig.11(d).

We had mentioned earlier that the success of the MGOC frameworks comes from learning an extended parameter (\mathcal{LP}) space, but the following discussion shows that this is true only in the presence of a nonlinear function as part of the mapping. In the DMD (4-MLOC- $\mathcal{I}1$) framework, there are 9 learning parameters in Θ to predict the limit cycle dynamics as compared to 27 parameters for 6-MGOC- $\mathcal{I}1$ architecture. However, in the absence of an nonlinear function in the convolution maps, the linear operator computed from the two methods are the same, i.e. the product of the different Θ_l for $l = 1 - 3$ in the 6-MGOC will trivially turn out to be the same as Θ learned from the DMD (4-MLOC- $\mathcal{I}1$) framework. In Fig.11, we use 4-cycles of (124 points) data in the limit cycle region for training and predict upto 17 cycles (527 data points). We see that the predictions obtained using 4-MLOC- \mathcal{I} and 6-MGOC- \mathcal{I} in Fig.11(a) and (b) are similar as the same linear transition operator Θ is estimated. However, with limited training data, the predictions start to diverge from the truth over large times as is clearly seen from the evolution of the third POD feature, a_3 .

While the addition of nonlinear functions in the convolution map aids the prediction of nonlinear dynamics, employing this formulation with a local optimization of the \mathcal{LP} does not always guarantee good results. We see an illustration of this in the performance of the 6-MLOC-TS1 architecture as seen from Fig.11(c), where all the three input features are incorrectly predicted in contrast to predictions by the 6-MGOC-TS1 in Fig.11(d). The prediction error quantifications for the limit-cycle regime in the training and prediction regions are shown in the first two rows of the table 2. These show that the linear DMD (4-MLOC-

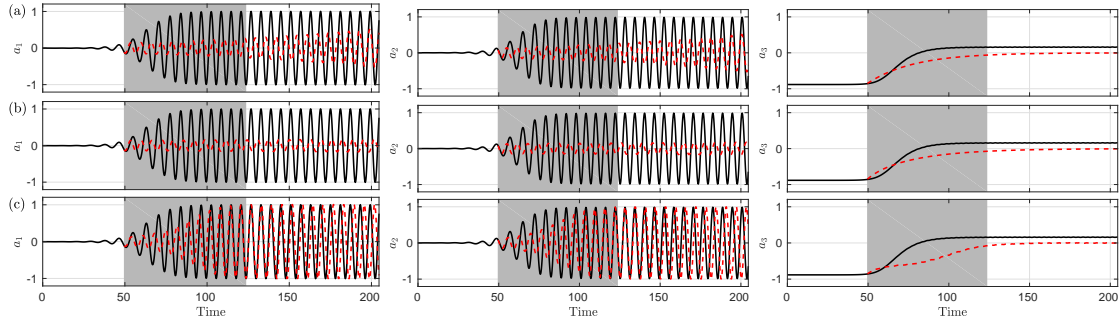


Fig. 12: Times series of predicted POD features obtained from (a) 4-MLOC- \mathcal{I} 1, (b) 6-MLOC-TS1 and (c) 6-MGOC-TS1 for TR-I as training region.

\mathcal{I}) architecture and the FFNN-like 6-MGOC-TS architecture produce error magnitudes of 7.4×10^{-3} and 1.6×10^{-2} respectively outside the training region. However, these errors are higher than the $O(1e^{-4})$ errors in the training region as one would expect. In spite of having larger errors in the prediction regime, the MGOC models do not allow for growth in error which is a desirable feature. As additional benchmarks we also include prediction errors for other architectures including 6-MLOC-P2, 6-MGOC-TS1 and 6-MGOC-TS3 which generate comparable prediction accuracy with 6-MLOC-P2 being the smallest. In summary, except for the EDMD-TS (6-MLOC-TS1) all the other models display reasonable accuracy for this limit-cycle dynamics in both the training and prediction regimes. However, we observe a gradual growth of the third feature in all the models except the 6-MGOC-TS architectures which can impact long-time predictions. It is for this reason we consider the MGOC architectures to perform the best within this regime.

Train cycles	\mathcal{E}	4-MLOC- \mathcal{I}		6-MLOC-TS		6-MLOC-P		6-MGOC-TS			
		$N_f = 1$	$N_f = 1$	$N_f = 1$	$N_f = 1$	$p = 2$	$p = 7$	$N_f = 1$	$N_f = 3$	$N_f = 9$	$N_f = 20$
16 – 20(LC)	\mathcal{E}_t	$1.6e^{-4}$		$3.3e^{-2}$		$6.7e^{-5}$	--	$2.7e^{-4}$	$2.1e^{-4}$	--	--
	\mathcal{E}_p	$7.4e^{-3}$		0.269		$3.5e^{-4}$	--	$1.6e^{-2}$	$8.1e^{-3}$	--	--
08 – 20(TR-I)	\mathcal{E}_t	0.417		0.467		0.475	$6.4e^{-6}$	0.320	$3.7e^{-2}$	$1.9e^{-2}$	$2.1e^{-2}$
	\mathcal{E}_p	0.513		0.483		0.776	$3.9e^{-4}$	0.686	0.146	0.153	0.148
04 – 16(TR-II)	\mathcal{E}_t	0.246		0.238		0.223	0.191	--	0.106	0.182	0.385
	\mathcal{E}_p	0.551		0.530		0.683	0.977	--	0.883	0.948	0.720

Table 2: Prediction error estimates for layer-wise local (MLOC) and global optimization methods (MGOC) for $Re = 100$.

3.5 Learning and Prediction of a Transient Cylinder Wake Dynamics

In the earlier section, we highlighted the role of the choice of nonlinearity and the importance of combining this with a GOC framework for stable long-time predictions. In this section, we focus on learning from transient wake flow data and predict the resulting limit-cycle system. It is well known that DMD (4-MLOC- \mathcal{I}) performs better on limit cycle problems and under performs in the transient regime due to its inability to handle the enhanced nonlinearity of the underlying dynamical system. In particular, if the limit-cycle dynamics represents a nonlinearity of order k then the transient wake regime corresponds to a nonlinearity of order $\geq k + 1$ [19]. Consequently, models that incorporate nonlinearity in the convolution maps such as the EDMD with polynomial basis [13] (or equivalently the 6-MLOC-P as adopted in this article) or the corresponding kernel representation [32] perform better for such problems, but only when using significant number of input features. In this section, we show that global optimization with nonlinear multilayer convolution provides much better learning and prediction capabilities from as little amount of input data as three features which the minimum amount of data one needs to capture the wake instability behind a cylinder [19].

For this analysis, we used two training regions in the unstable transition regime, namely transient region-I (TR-I) and transient region-II (TR-II) as shown in figure 10a corresponding to 8 – 20 and 4 – 16 cycles respectively with both regions consisting of 372 data points. TR-I is relatively less challenging as almost all of the training data incorporates vortex shedding, but with an amplitude that is growing. In

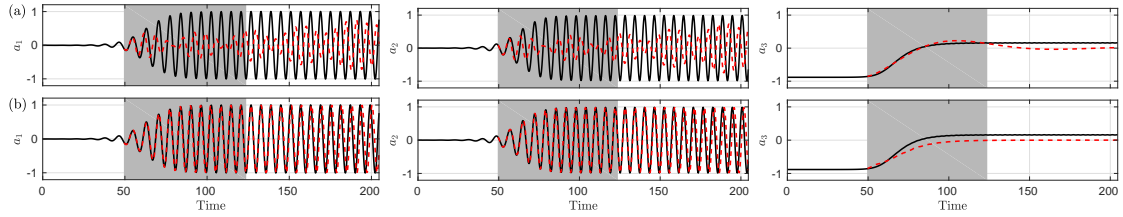


Fig. 13: Times series of predicted POD features obtained from (a) 6-MLOC-P2, (b) 6-MGOC-TS3 for TR-I as training region.

TR-II the first 30% of the training data includes a stable wake with symptoms of instability that grows in amplitude all through the regime. This has implications for predictions using machine learning models where the training data almost always determines what kind of dynamics the model can predict. If one were to rank the level of difficulty in predicting the resulting limit-cycle dynamics from different sets of training data then the most difficult would be TR-II followed by TR-I and lastly, the limit-cycle training data used in the previous section.

Figure 12 shows the predictions obtained from the different locally optimal 4-MLOC- $\mathcal{I}1$ (DMD), 6-MLOC-TS1 (EDMD-TS1) and the FFNN-like globally optimal 6-MGOC-TS1 methods for the TR-I training region. We can see that, all these methods fail to learn the nonlinear dynamics and predict the resulting limit-cycle system to varying levels of inaccuracy - MGOC being the closest. This can be attributed to the lack of sufficient nonlinearity in the models and insufficient learning parameters to represent the dynamics. It is worth pointing out that the EDMD-TS (6-MLOC-TS1) does not extend the \mathcal{LP} space as against its polynomial basis variant, EDMD-P2 (6-MLOC-P2). Also, the choice of P2 basis is physics-driven to account for the quadratic nonlinearity of the POD features as embedded within the Navier-Stokes equations that describe the flow. On the other hand, for the MGOC methods, a logical way to extend the \mathcal{LP} space is to increase the number of features in the intermediate layers by increasing N_f . Consequently, we use 6-MLOC-P2 (EDMD-P2) as the baseline case and design a MGOC architecture with similar sized \mathcal{LP} space with feature factor, $N_f = 3$. This approach of choosing N_f based on the dimension of the quadratic polynomial features is a logical way to design FFNN-like MGOC architectures as against more *ad hoc* choices. A schematic comparing the four intermediate layers in the 6-MLOC-P2 and the 6-MGOC-TS3 architectures is shown in Fig.5. For 6-MLOC-P2, the three input POD features are mapped onto a polynomial basis space with nine features. In 6-MGOC-TS3, the three input features are mapped onto an unknown basis space, but guaranteed to be optimal for the chosen architecture. In this spirit of exploration, we also try a 7^{th} -order polynomial feature map, i.e. a 6-MLOC-P7 and corresponding MGOC architectures with an expanded \mathcal{LP} space ($N_f = 9$ and 20) to assess the effect of \mathcal{LP} dimensionality on the predictions.

Figure 13 shows the predictions from 6-MLOC-P2 and 6-MGOC-TS3 using TR-I data. In spite of the embedded quadratic nonlinearity, the 6-MLOC-P2 framework fails to predict the correct limit-cycle dynamics using just three input features. On the other hand, 6-MGOC-TS3 with a similar architecture with global optimization learns and predicts the flow dynamics more accurately. These prediction error trends are quantified in table 2. This is consistent with our earlier discussions that a larger \mathcal{LP} dimension improves predictions as 6-MGOC-TS3 learns 135 parameters compared to 81 for the 6-MLOC-P2 case. Although these numbers are not vastly different, the 6-MLOC-P2 fails to even predict qualitatively accurate results. It is also worth noting that 6-MGOC-TS3 predicts the first two POD features accurately (see fig. 13), but the third coefficient is biased towards a zero magnitude. We have found that this is due to the absence of bias term which when incorporated into the MGOC architectures corrects for this error as discussed and shown in fig. 25 included in Appendix A.

As a reference, prior work [14] on locally optimal architectures (6-MLOC-P2) has shown that 50 input features, 1325 quadratic nonlinear features with \mathcal{LP} dimension of $1.7e^6$ can generate accurate predictions, thus indicating the need for a much larger \mathcal{LP} dimension. Here, we explore whether expanding the \mathcal{LP} dimension with just 3 input features improves the model performance. We accomplish this by increasing the order of polynomial to 7^{th} -degree i.e. we consider a 6-MLOC-P7 architecture method with 3 POD features and a \mathcal{LP} dimension of 15,625- a nearly ≈ 200 factor increase. Increasing the \mathcal{LP} dimension by a couple of orders of magnitude produces accurate predictions of the nonlinear dynamics as shown in fig. 14a. We note that choices of polynomial smaller than degree seven did not produce accurate predictions. We also explore the effect of increasing the \mathcal{LP} dimension for the MGOC architectures by changing N_f as shown in table 1. The predictions obtained using 6-MGOC-TS9 and 6-MGOC-TS20 (see Figs.14(b) and (c)) with \mathcal{LP} dimensions of 891 and 3960 respectively (factors of ≈ 10 & 40) also showed improved performance and compare favorably to the 6-MLOC-P7 architecture. However, both these GOC variants show similar results indicating that performance improvements have saturated, possibly due to the non-inclusion of the bias term

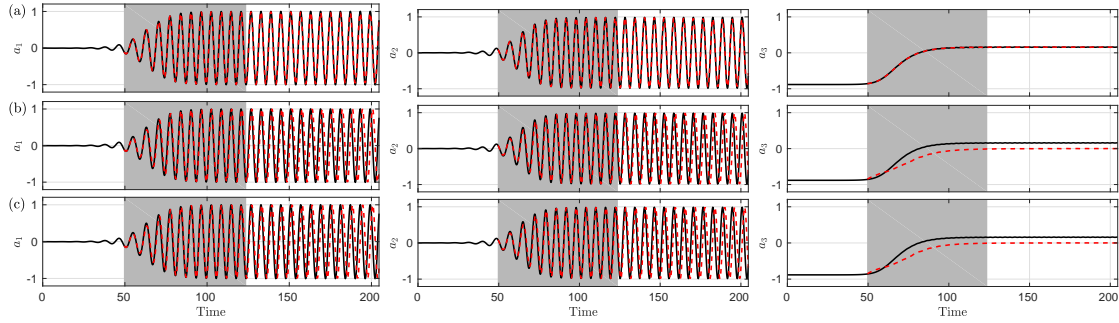


Fig. 14: Times series of predicted POD features obtained from (a) 6-MLOC-P7, (b) 6-MGOC-TS9 and (c) 6-MGOC-TS20 for TR-I as training region.

(Appendix A). Summarizing, for both the MLOC and MGOC architectures, increasing the \mathcal{LP} dimension improves learning and prediction performance. However, MGOC requires relatively modest increases in \mathcal{LP} dimension as compared to MLOC methods which provides them an advantage. In a way, this result reinforces the underlying principles behind the success of deep learning architectures [30]. The MLOC can be viewed as a two-layer shallow learning architecture requiring larger intermediate layer dimensions while the MGOC is its deep learning counterpart requiring smaller number of intermediate layer features, but layered over each other.

We use the same modeling architecture's 6-MLOC-P2, 6-MLOC-P7 along with 6-MGOC-TS3, -TS9, -TS20 on the more challenging TR-II data and the resulting predictions of the POD features are shown in figures 15 and 16. In this case both the MLOC architectures, i.e. 6-MLOC-P2 and 6-MLOC-P7 perform inadequately in spite of the extended \mathcal{LP} space. On the other hand, predictions obtained using 6-MGOC-TS offer better qualitative results and predict the limit cycle dynamics, but display perceptible quantitative inaccuracy without a bias term and is insensitive to extension of learning parameter space (see table 2). However, as before, we observe that this quantitative inaccuracy, especially in the third POD feature is mitigated through the inclusion of a bias term as the plots clearly show in fig. 26 in Appendix A.

We note that computing the error metrics using a simple L_2 norm do not always represent the observed qualitative nature of the predictions accurately for such repetitive limit-cycle dynamics. For example, the predictions which qualitatively learn the dynamics but with a phase error tend to show larger errors than some of the non-qualitative predictions. The other aspect worthy of mention is that learning of all the MLOC/MGOC models is based on learning the 'local' errors and not the global errors that takes into account error propagation using predictions. Such a 'local' cost function misleads the learning process as the minimization of (\mathcal{J}) does not reflect minimization in prediction errors. To illustrate, in table 2, although the cost functions (\mathcal{J}) in most of the methods considered here are reduced to $O(1e^{-6})$, the associated prediction errors are of $O(1e^{-1})$. Improved regularization methods that use Jacobian of the cost function have been proposed in [46] and will need to be explored.

To relate the observed deviation in the POD features to the predicted flow field of interest, we show in Fig.17 the reconstructed solution (i.e. the actual predicted state vector) for $Re = 100$ obtained using the different methods considered in this paper. These plots are generated based on learning and prediction using TR-I (*cycles* : 8 – 20) data, and shown at $\approx T = 86.2$ (first column) which is the midpoint of the training region. Columns 2 and 3 in Fig.17 represent predictions at $T = 124$, the last point in TR-I and $T = 205$, the last point in the prediction regime. These results clearly show that the MLOC methods with low \mathcal{LP} dimension such as 4-MLOC-Z1, 6-MLOC-TS1 and 6-MLOC-P2 show delayed onset of wake instability and incorrect vortex shedding while the 6-MGOC-TS1 predicts the instability growth more accurately.

In summary, one or more strategies of extending the \mathcal{LP} space, learning the parameters using a global optimization and improved regularizations help enhance the efficiency of the learning process and accuracy of the resulting predictions only when sufficient data is available. These strategies work much better with the TR-I data as against the TR-II. For the TR-II regime, the limited quantity of information about the limit-cycle dynamics in the training data is harder to overcome by the design of the machine learning architecture. Fortunately, in this case the MGOC architectures offer a significant improvement over MLOC, for a given \mathcal{LP} dimension (computational cost), especially with the inclusion of a bias term.

3.5.1 At different Reynolds Number

In the previous section we show the importance of training data quality (i.e. relevance to the data we are trying to predict) for MLOC methods while MGOC methods are relatively more robust to the data

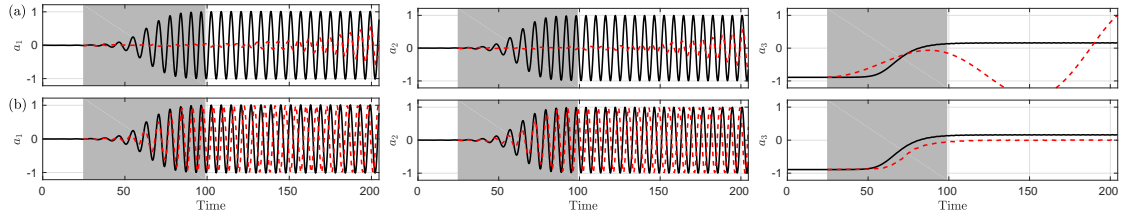


Fig. 15: Times series of predicted POD features obtained from (a) 6-MLOC-P2, (b) 6-MGOC-TS3 for TR-II data.

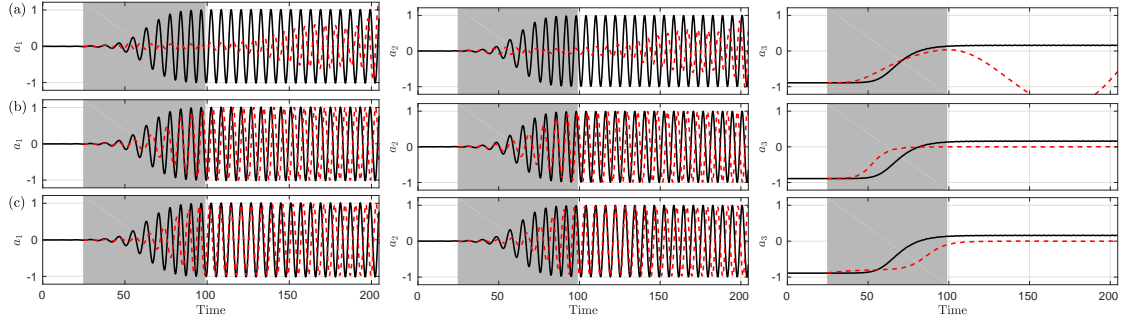


Fig. 16: Times series of predicted POD features obtained from an extended \mathcal{LP} space (a) 6-MLOC-P7, (b) 6-MGOC-TS9 and (c) 6-MGOC-TS20 for TR-II data.

regime chosen for training. In this section, we explore briefly the impact of the inherent dimensionality of the system by considering a different flow Reynolds number, $Re = 1000$. In this case the first three POD features represent 90% of the total energy (figure 7(a)) as against 95% for $Re = 100$ flow. The phase portrait for the first three modes is shown in figure 7(b) which indicates the dynamics transitioning into a limit cycle much faster than observed for $Re = 100$. For the data-driven modeling assessment, we once again choose two different training regimes with different proportion of transient and limit-cycle information in the data as shown in fig. 10b. The predictions for the different MLOC and MGOC models for both TR-I and TR-II regimes are shown in figures 18, 19 and 20 with quantifications reported in table 3. As observed for the low Reynolds number case, the MGOC architectures perform better than the MLOC architecture in the TR-I regime for the similar \mathcal{LP} dimensions as shown in fig. 18. With increase in the \mathcal{LP} dimension, the 6-MLOC-P7 or EDMD-P7 framework shows much improved accuracy (in fig. 19 relative to the 6-MLOC-P2 while the MGOC performance improvement has saturated. The bias that shows up in the third POD feature for the MGOC models goes away when adopting a non-zero bias term in the architecture as shown in fig. 27 in Appendix A.

Moving on to the more challenging TR-II regime in fig. 20, the 6-MLOC-P7 framework performs poorly although it made accurate predictions for the TR-I data. The different MGOC with large number of learning parameter, \mathcal{LP} , also perform poorly (see fig. 20), but capture the overall qualitative behavior such as the dynamics settling into a limit cycle. However, predicted growth of the wake instability is faster than that for the true data. This is easily seen from table 3 where the prediction errors for the MGOC methods is greater than or comparable to the prediction errors. Unlike in the previous instances, these predictions do not improve with the addition of a bias unit as shown in fig. 28 in Appendix A. The prediction inaccuracies for this high Reynolds number case points to the possibility of the data missing dynamically relevant information contained in the lower energy containing POD modes. However, in practice, this is a realistic representation of the available data quality with the smaller scale features often not resolved with sufficient resolution.

3.6 Learning and Prediction of a Transient 2D Buoyant Boussinesq Mixing Flow

Unlike the low-dimensional limit-cycle attractor modeled in the earlier sections, here we explore a non-stationary and higher-dimensional buoyant Boussinesq mixing flow discussed in sec. 3.1.2. In fact, we observed previously that prediction of the transient evolution of the cylinder wake dynamics before it stabilizes into a limit-cycle is highly sensitive to the choice of training data. In addition, learning and predictability of these dynamics are also dependent on the flow data capturing sufficient dynamics for

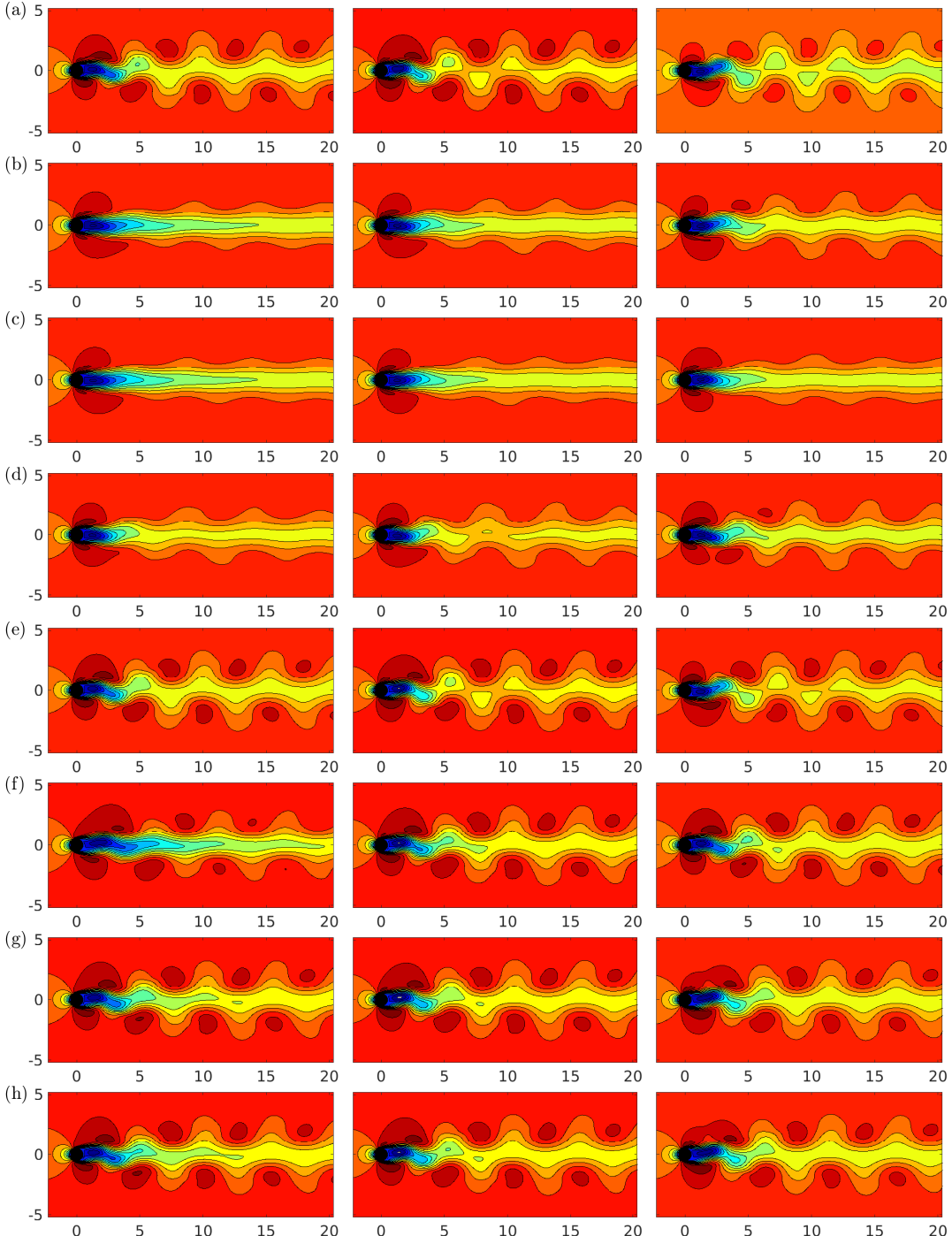


Fig. 17: Reconstruction of $Re100$ flow field based on predicted POD features obtained from (a) Actual data, (b) 4-MLOC- $\mathcal{I}1$ (c) 6-MLOC-TS1 (d) 6-MLOC-P2 (e) 6-MLOC-P7 (f) 6-MGOC-TS1 (g) 6-MGOC-TS3 (h) 6-MGOC-TS9 comparison with 15 equally spaced contour levels ranging between $(-0.2645, 1.2963)$.

Train cycles	\mathcal{E}	6-MLOC-P (EDMD-P)		6-MGOC-TS		
		$p = 2$	$p = 7$	$N_f = 3$	$N_f = 9$	$N_f = 20$
06 – 18	\mathcal{E}_t	0.373	$2.6e^{-4}$	$1.5e^{-2}$	$2.6e^{-2}$	$3.8e^{-2}$
	\mathcal{E}_p	0.851	$2.6e^{-4}$	0.330	$2.2e^{-2}$	$9.7e^{-2}$
02 – 14	\mathcal{E}_t	0.320	0.191	0.379	0.695	0.606
	\mathcal{E}_p	3.414	0.375	0.183	0.395	0.654

Table 3: Prediction error estimates for layer-wise local (MLOC) and global optimization methods (MGOC) for $Re = 1000$

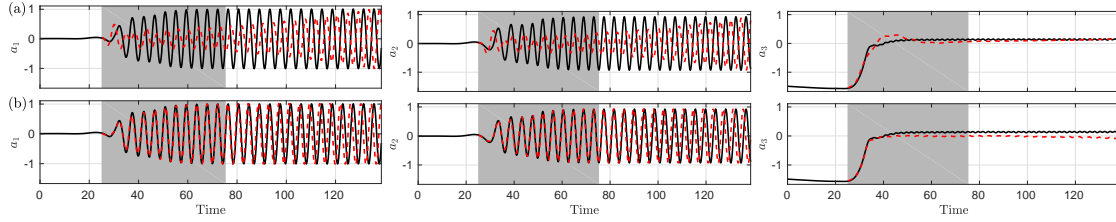


Fig. 18: Time series comparison plot of the predicted POD features with the original data for TR-I data using different MLOC and MGOC modeling frameworks. (a) 6-MLOC-P2 (EDMD-P2) and (b) 6-MGOC-TS3.

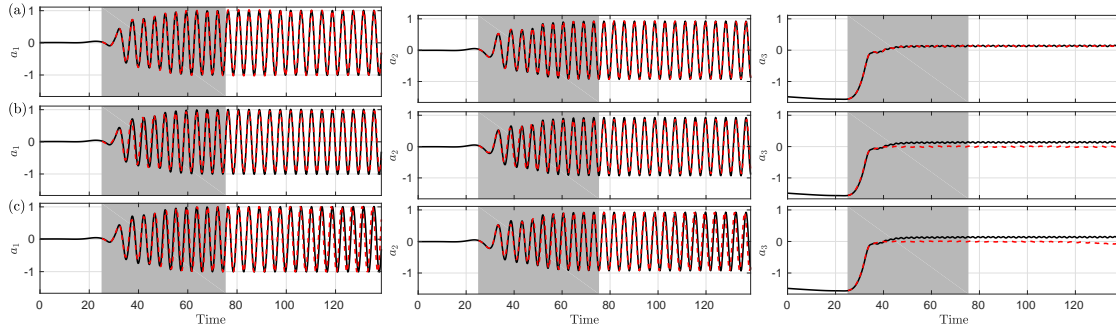


Fig. 19: Time series comparison plot of the predicted POD features with the original data for TR-I data using different MLOC and MGOC modeling frameworks. (a) 6-MLOC-P7 (EDMD-P7), (b) 6-MGOC-TS9 and (c) 6-MGOC-TS20.

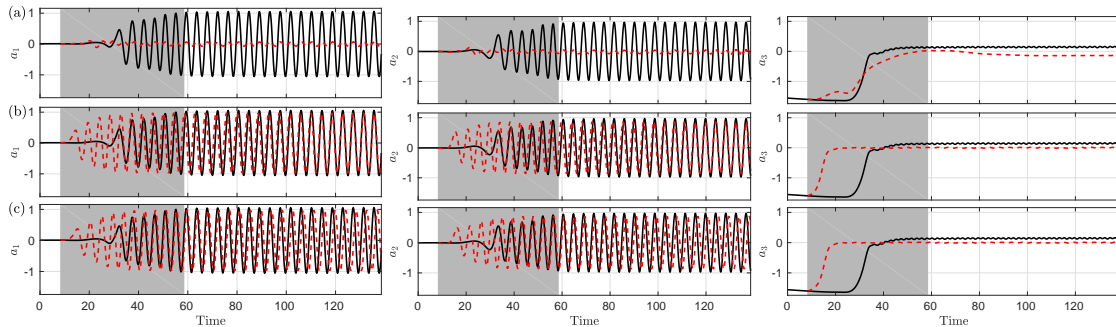


Fig. 20: Time series comparison plot of the predicted POD features with the original data for TR-II data using different MLOC and MGOC modeling frameworks. (a) 6-MLOC-P7 (EDMD-P7), (b) 6-MGOC-TS9 and (c) 6-MGOC-TS20

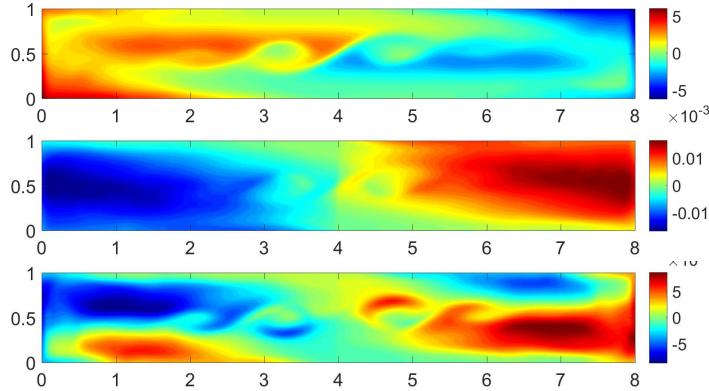


Fig. 21: Visualization of the first three POD basis (in decreasing order of energy content) used to model the dynamics with the data-driven models.

accurate prediction. For this study, we chose to retain just 80% of the total energy of the system captured in the CFD generated data (similar to a low resolution measurement) resulting in just 3 POD features in the 2nd layer of the MLOC/MGOC architecture. Sensitivity to these aspects is stronger when trying to predict non-stationary phenomena that may settle into an unknown attractor over long times. The training data is almost always sparse for such dynamics and may not overtly show any evidence of the existence of such an attractor. Such instability-driven non-stationary problems are challenging for data-driven techniques that do not leverage knowledge of the underlying governing system and employ black box machine learning. Even if one were to diversify the training data-set with multiple realizations of the system, performance improvements are not guaranteed as the underlying dynamics will be different. We choose a single realization of such a data-sparse and low-dimensional representation of system for assessment of the MLOC and MGOC architectures .

For this case study, we consider the following locally optimal methods 4-MLOC- \mathcal{I} (DMD), 6-MLOC-TS (EDMD-TS) and 6-MLOC-P (EDMD-P). We contrast these with the following globally optimal 6-MGOC-TS with growing \mathcal{LP} dimensions for $N_f = 1, 3, 5$. As a preliminary step, we use the entire available data for training and assess the reconstruction performance of these models. Figure 22 compares the results for the linear 4-MLOC- \mathcal{I} (DMD) model with the nonlinear 6-MLOC-TS1 (EDMD-TS1) and 6-MGOC-TS1 (EDMD-P) models with small number of learning parameters (9 and 27 respectively). Contrary to findings from the earlier section, all the LOC models including the linear DMD and EDMD with tansigmoid nonlinearity (EDMD-TS1) compare favorably to the GOC models with $N_f = 1$. All three models fail to predict the dynamics of the third POD feature which represents the secondary eddies from the Kelvin-Helmholtz instability generated by the mixing layer dynamics (see bottom plot in fig. 21). The LOC models generate slightly better outcomes as compared to the MGOC(FFNN) for the first two POD features that represent transverse and vertical mixing (top two plots in fig. 21). To improve the predictions of the third POD feature, we expand the learning parameter (\mathcal{LP}) dimension by comparing 6-MLOC-P3 (EDMD-P3), 6-MGOC-TS3 and 6-MGOC-TS5 as shown in fig. 23. Consistent with earlier observations, this increase in \mathcal{LP} improves the prediction of the third feature for both the MLOC and MGOC methods with MLOC performing better. Similar performance was also realized with the EDMD-P2 (6-MLOC-P2) architecture and is not reported here for brevity. This shows that for reconstructing the dynamics, MLOC methods are more accurate as compared to the globally optimal FFNNs. This can be attributed to the choice of nonlinear mapping involved in MGOC architectures and exploration of other transfer functions is beyond the scope of this study.

To assess the ability of the models to learn the underlying system dynamics, we split the dataset equally into training and prediction regimes. Figure 24 compares the predicted output of the three POD features for 6-MLOC-TS1, 6-MLOC-P2 and 6-MGOC-TS3. For all the models, we clearly observe that reconstruction is better than prediction performance. So we focus on the latter in this discussion. The globally optimal FFNN (6-MGOC-TS3) outperforms the two LOC model architectures considered here in terms of stability and accuracy. Particularly, the MGOC prediction using 50% data (fig.24c) is highly similar to that using the entire dataset as the reconstruction experiment shown in fig. 23c. This shows that these models offer robust and stable performance even with limited data. In summary, we see that MLOC methods offer competitive reconstruction performance, but MGOC models across the different architectures offer stable and robust model performance for long time predictions using limited data.

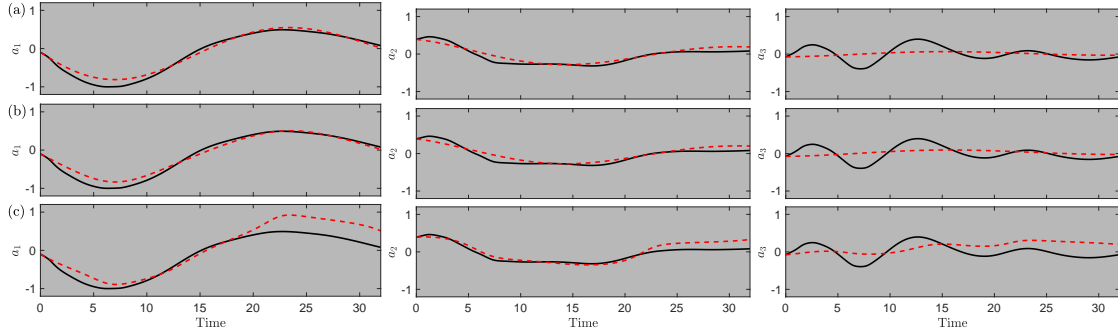


Fig. 22: Times series comparison plot of the 3 POD weights with the original data with entire data used for training (a)4-MLOC-\$\mathcal{I}1\$ (DMD or 6-MLOC-P1) , (b) 6-MLOC-TS1 and (c) 6-MGOC-TS1

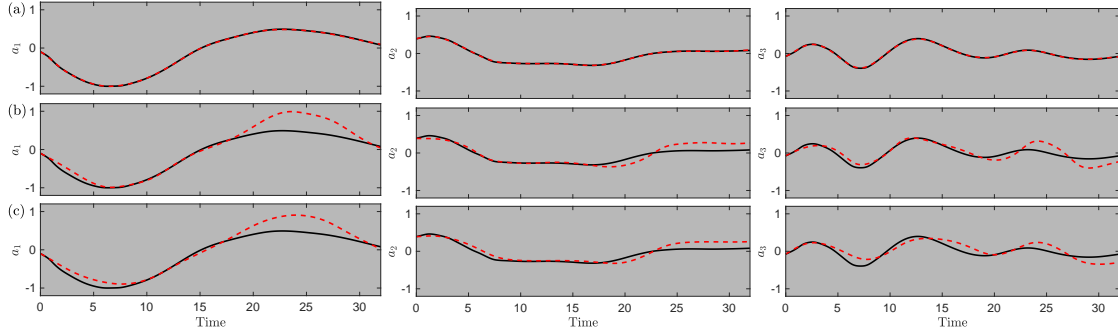


Fig. 23: Times series comparison plot of the 3 POD weights with the original data with complete data used for training (a) 6-MLOC-P3 (EDMD-P3) , (b) 6-MGOC-TS3 and (c) 6-MGOC-TS5

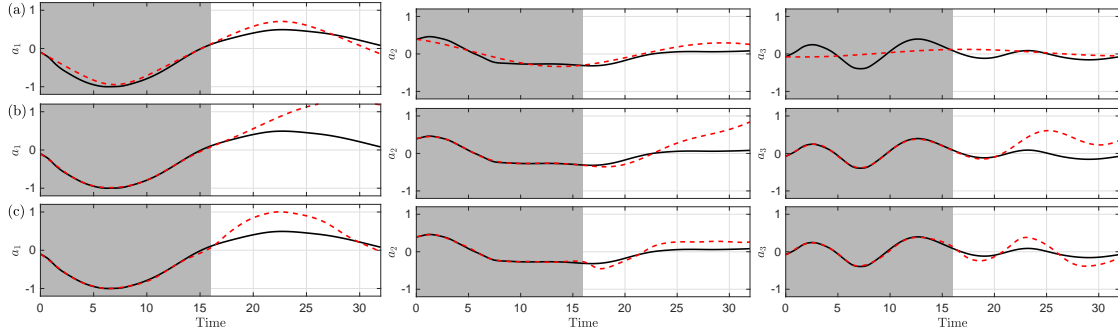


Fig. 24: Times series comparison plot of the 3 POD weights with the original data with half data used as training (a) 6-MLOC-TS1 , (b) 6-MLOC-P2 and (c) 6-MGOC-TS3

4 Discussion and Summary

In this article we explore the role of local (MLOC) versus global optimization (MGOC) of the multilayer convolution maps through the lens of learning parameter dimensionality and nonlinear transfer functions on their ability to reconstruct and predict over long times the transient, nonlinear dynamics of canonical fluid flows. Fluid flows represent multiscale PDE dynamical systems that often require low-dimensional data-driven representations and evolutionary models for a multitude of applications. The locally optimal multilayer frameworks allow for both backward and forward operations and can support symmetric architectures including Koopman approximation methods such as DMD and EDMD. Such approaches allow for spectral analysis of the underlying system in addition to building data-driven models. On the other hand, globally optimal (MGOC) frameworks can support only forward maps due to the choice of gradient-based optimization algorithms being commonly used as the tool of choice for nonlinear parametric regression in machine learning. Consequently, MGOC architectures like FFNN cannot learn the Koopman operator using current methods. Recent work by the authors on leveraging feedback networks [33] with feedforward

networks has allowed us to bypass this limitation to perform Koopman spectral analysis along with building an effective predictive model.

The success of both the MLOC and MGOC architectures are tied to the nonlinearity in the mapping and the size of the learning parameter space in the multilayer architecture design. We observe that for prediction of limit-cycle dynamics from limit-cycle data where all the different models show reasonable success, FFNN-like MGOC models control the growth of long-time prediction errors better than MLOC models. While prediction errors decrease with increase in dimension of the learning parameters and the appropriateness of the nonlinear transfer function, their combination through a MGOC architecture turned out to be the most effective. As an example of appropriateness of the nonlinear transfer function, we show that tansigmoid functions operate well with MGOC architectures as against MLOC architectures which perform better using polynomial nonlinear features.

To assess the ability of these model architectures to generalize to diverse training data regimes, we considered two different case studies with different training regimes that differ in their limit-cycle content. In order to mimic the availability of only limited resolution data as is commonly the case, we chose to train these models using their low-dimensional representation with only three POD features. Within the context of these restrictions, we observed that for comparable number of learning parameters, the FFNN-like MGOC architectures outperform the corresponding locally optimal MLOC model frameworks by a significant margin in terms of accuracy and robustness. To illustrate this, we show that the 6-MGOC-TS1 architecture with 9 learning parameters produce qualitatively accurate results as against the grossly inaccurate results using DMD/EDMD (4-MLOC and 6-MLOC) models. With increase in \mathcal{LP} dimension, both class of methods converge to the accurate predictions with tangible improvements and slower convergence in the MLOC as compared to the MGOC framework. For example, a 7th polynomial nonlinearity in the MLOC architecture with $O(1.5 \times 10^4)$ parameters produced accurate predictions as against the 6-MGOC-TS3 models with a bias term (traditional FFNN) with just 135 parameters.

The downside of MGOC models is their computational cost and learning time as one needs to solve a nonlinear regression problem, often requiring iterative gradient search based algorithms which can also impact convergence. A common issue with FFNN/MGOC architectures is the solution being stuck in a local minimum as against a true global minimum for which algorithmic advances continue to be explored. However, this is made up for by the relatively modest increase in \mathcal{LP} dimension needed to improve the learning and prediction performance. The case with limited quantity of information about the limit-cycle dynamics in a different training data regime (TR-II regime) both class of methods find learning and prediction harder. In this case however, the MGOC architectures were able to generate accurate predictions with as little as 135 parameters especially with the inclusion of a bias term whereas the MLOC method with $O(1.5 \times 10^4)$ parameters failed to predict meaningful data. When the inherent system dimension increases at higher Reynolds numbers, i.e. $Re = 1000$, the above trends remain consistent, but the dynamics are harder to predict, especially when the dimension of the training data is not increased. In spite of using data with missing dynamically relevant physics, the FFNN/MGOC models produced stable and qualitatively accurate results. We also explored data-driven modeling of data-sparse non-stationary buoyant mixing flow phenomena in the context of pure learning-based reconstruction and learning-based prediction. For such systems, the MLOC-based methods turned out to be good at reconstruction (consistent with [14]), but struggle to learn the dynamics to predict a future state accurately. While both methods struggle with quantitatively accurate prediction of such data, the MGOC frameworks generate better qualitative accuracy in the prediction regime.

In summary, the strategy of extending the \mathcal{LP} space, learning the model parameters concurrently using a global optimization and improved regularizations [46] can help enhance the efficiency of the learning process, improve robustness and accuracy of the resulting predictions. However, as with machine learning in general, these outcomes are strongly tied to data sufficiency and quality. Consistently, we observe that the MGOC models such as FFNN outperform the suite of MLOC frameworks explored in this article, although they are slightly harder to train. We see MLOC models as two-layer shallow learning architectures requiring large intermediate layer dimensions while the MGOC is its deep learning counterpart that while harder to train can approximate the nonlinear dynamics using a few parameters. Their success in long-time prediction using higher-dimensional input features is yet to be explored although improved nonlinear convex and non-convex optimization algorithms that can operate efficiently on GPU hardware make it feasible.

Acknowledgements We acknowledge support from Oklahoma State University start-up grant and OSU HPCC for compute resources to generate the data used in this article. The authors thank Chen Lu, a former member of the Computational, Flow and Data science research group at OSU for providing the CFD data sets used in this article. BJ acknowledges discussions on data-driven modeling with Prof. Karthik Duraisamy at the University of Michigan.

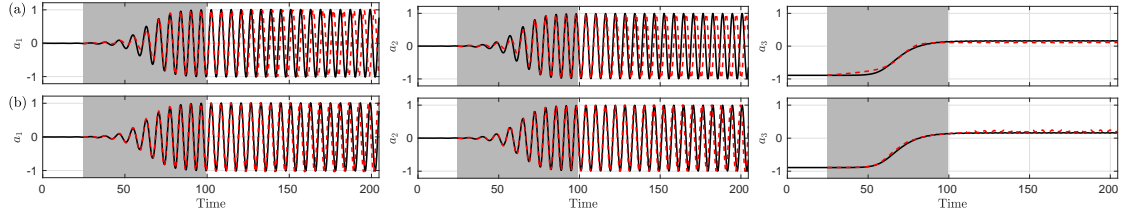


Fig. 26: Times series of predicted $Re=100$ POD features obtained from (a) 6-MGOC-TS3 and (b) 6-MGOC-TS9 compared with their respective original coefficients for TR-II region.

Author Contribution

BJ conceptualized the work with input from SCP. SCP developed the data-driven modeling codes used in this article with input from BJ. BJ and SCP analyzed the results. BJ finalized the writing of the manuscript with a first draft from SCP.

A Effect of Bias on Predictions

The results presented in the main sections of this article were based on FFNN-like MGOC architectures devoid of the bias term. It is well known from machine learning literature [36] that the presence of the bias term contributes significantly to the universal function approximation characteristic of FFNNs provided sufficient L^p norms are used to capture the dynamics. The lack of a bias parameter impacts the predictions of the shift mode for the transient cylinder wake dynamics (section 3.5). In contrast, the modes with zero mean were predicted accurately. The bias term helps in quantitative translation (shift) of the learned dynamics into higher or lower values as the case may be. In this additional discussion we provide predictions obtained with a non zero bias term. In figs. 25 and 27, we have plotted the predictions obtained from 6-MGOC-TS1, -TS3, TS9 with TR-I for $Re = 100$ and $Re = 1000$ respectively. And, in figs. 26 and 28, the predictions obtained from 6-MGOC-TS3 and -TS9 with the TR-II data. In these cases, we see that the shift mode (third POD feature) is predicted accurately with the bias term. Alternatively, one can preprocess the input data such that their mean values are zero.

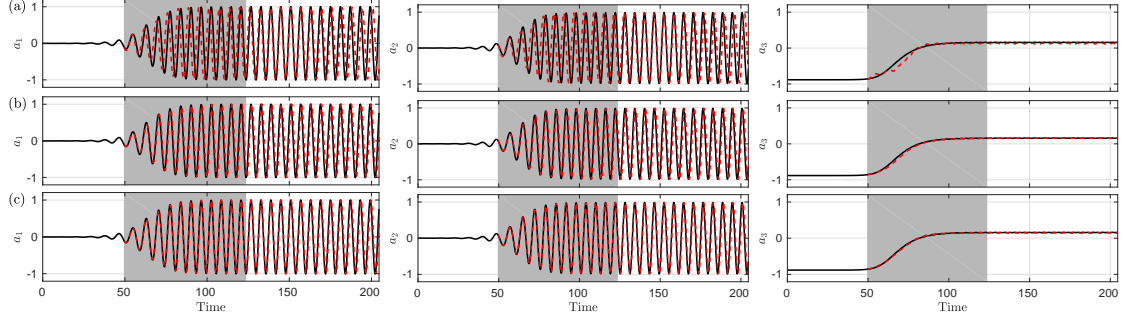


Fig. 25: Times series of predicted $Re=100$ POD features obtained from (a) 6-MGOC-TS1 (b) 6-MGOC-TS3 and (c) 6-MGOC-TS9 compared with their respective original coefficients for TR-I region.

References

1. A. M. Edstrand, P. J. Schmid, K. Taira, and L. N. Cattafesta, “A parallel stability analysis of a trailing vortex wake,” *Journal of Fluid Mechanics*, vol. 837, pp. 858–895, 2018.
2. X. Wu, P. Moin, J. M. Wallace, J. Skarda, A. Lozano-Durán, and J.-P. Hickey, “Transitional–turbulent spots and turbulent–turbulent spots in boundary layers,” *Proceedings of the National Academy of Sciences*, p. 201704671, 2017.
3. E. A. Deem, L. N. Cattafesta, H. Yao, M. Hemati, H. Zhang, and C. W. Rowley, “Experimental implementation of modal approaches for autonomous reattachment of separated flows,” in *2018 AIAA Aerospace Sciences Meeting*, p. 1052, 2018.
4. J. Kim and T. R. Bewley, “A linear systems approach to flow control,” *Annu. Rev. Fluid Mech.*, vol. 39, pp. 383–417, 2007.
5. S. L. Brunton and B. R. Noack, “Closed-loop turbulence control: progress and challenges,” *Applied Mechanics Reviews*, vol. 67, no. 5, p. 050801, 2015.
6. Y. Cao, J. Zhu, I. M. Navon, and Z. Luo, “A reduced-order approach to four-dimensional variational data assimilation using proper orthogonal decomposition,” *International Journal for Numerical Methods in Fluids*, vol. 53, no. 10, pp. 1571–1583, 2007.

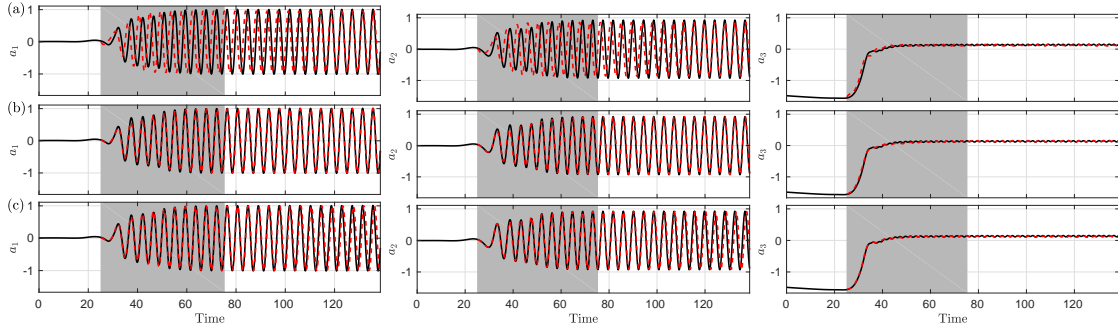


Fig. 27: Times series of predicted $Re1000$ POD features obtained from (a) 6-MGOC-TS1 (b) 6-MGOC-TS3 and (c) 6-MGOC-TS9 compared with their respective original coefficients in the TR-I.

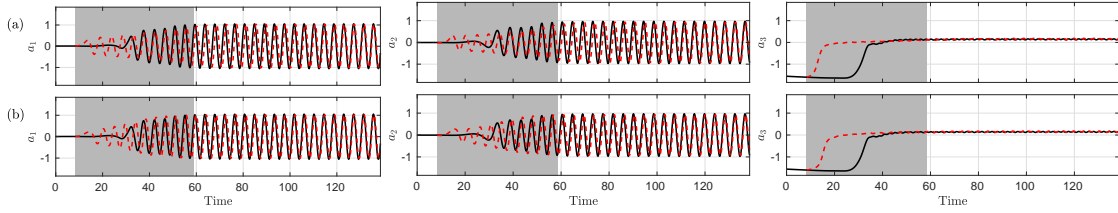


Fig. 28: Times series of predicted $Re1000$ POD features obtained from (a) 6-MGOC-TS3 and (b) 6-MGOC-TS9 compared with their respective original coefficients in the TR-II.

7. F. Fang, C. Pain, I. Navon, G. Gorman, M. Piggott, P. Allison, P. Farrell, and A. Goddard, “A pod reduced order unstructured mesh ocean modelling method for moderate reynolds number flows,” *Ocean modelling*, vol. 28, no. 1-3, pp. 127–136, 2009.
8. P. Benner, S. Gugercin, and K. Willcox, “A survey of projection-based model reduction methods for parametric dynamical systems,” *SIAM review*, vol. 57, no. 4, pp. 483–531, 2015.
9. S. Bagheri, “Koopman-mode decomposition of the cylinder wake,” *Journal of Fluid Mechanics*, vol. 726, pp. 596–623, 2013.
10. C. W. Rowley, I. Mezić, S. Bagheri, P. Schlatter, and D. S. Henningson, “Spectral analysis of nonlinear flows,” *Journal of Fluid mechanics*, vol. 641, pp. 115–127, 2009.
11. C. W. Rowley and S. T. Dawson, “Model reduction for flow analysis and control,” *Annual Review of Fluid Mechanics*, vol. 49, pp. 387–417, 2017.
12. P. J. Schmid, “Dynamic mode decomposition of numerical and experimental data,” *Journal of Fluid Mechanics.*, vol. 656, pp. 5–28, 2010.
13. M. O. Williams, I. G. Kevrekidis, and C. W. Rowley, “A data–driven approximation of the koopman operator: Extending dynamic mode decomposition,” *Journal of Nonlinear Science*, vol. 25, no. 6, pp. 1307–1346, 2015.
14. C. Lu, B. Jayaraman, J. Whitman, and G. Chowdhary, “Sparse convolution-based markov models for nonlinear fluid flows,” *arXiv preprint arXiv:1803.08222*, 2018.
15. J. L. Lumley, *Stochastic tools in turbulence*. Courier Corporation, 2007.
16. L. N. Trefethen and D. Bau III, *Numerical linear algebra*, vol. 50. Siam, 1997.
17. C. Lu and B. Jayaraman, “Data-driven modeling for nonlinear fluid flows,” in *23rd AIAA Computational Fluid Dynamics Conference*, no. 3628, pp. 1–16, 2017.
18. G. Berkooz, P. Holmes, and J. L. Lumley, “The proper orthogonal decomposition in the analysis of turbulent flows,” *Annual review of fluid mechanics*, vol. 25, no. 1, pp. 539–575, 1993.
19. B. R. Noack, K. Afanasiev, M. MORZYŃSKI, G. Tadmor, and F. Thiele, “A hierarchy of low-dimensional models for the transient and post-transient cylinder wake,” *Journal of Fluid Mechanics*, vol. 497, pp. 335–363, 2003.
20. C. Bishop, C. M. Bishop, *et al.*, *Neural networks for pattern recognition*. Oxford university press, 1995.
21. M. B. Christopher, *PATTERN RECOGNITION AND MACHINE LEARNING*. Springer-Verlag New York, 2016.
22. H. Wu and F. Noé, “Variational approach for learning markov processes from time series data,” *arXiv preprint arXiv:1707.04659*, vol. 17, 2017.
23. I. Mezić, “Spectral properties of dynamical systems, model reduction and decompositions,” *Nonlinear Dynamics*, vol. 41, no. 1, pp. 309–325, 2005.
24. B. O. Koopman, “Hamiltonian systems and transformation in hilbert space,” *Proceedings of the National Academy of Sciences*, vol. 17, no. 5, pp. 315–318, 1931.
25. J. J. Hopfield, “Neural networks and physical systems with emergent collective computational abilities,” *Proceedings of the national academy of sciences*, vol. 79, no. 8, pp. 2554–2558, 1982.
26. S. Hochreiter and J. Schmidhuber, “Long short-term memory,” *Neural computation*, vol. 9, no. 8, pp. 1735–1780, 1997.
27. R. Soltani and H. Jiang, “Higher order recurrent neural networks,” *arXiv preprint arXiv:1605.00064*, 2016.
28. R. Yu, S. Zheng, and Y. Liu, “Learning chaotic dynamics using tensor recurrent neural networks,” in *Proceedings of the ICML 17 Workshop on Deep Structured Prediction, Sydney, Australia, PMLR 70*, 2017.
29. Y. Bengio, P. Simard, and P. Frasconi, “Learning long-term dependencies with gradient descent is difficult,” *IEEE transactions on neural networks*, vol. 5, no. 2, pp. 157–166, 1994.
30. Y. Bengio, I. J. Goodfellow, and A. Courville, “Deep learning,” *Nature*, vol. 521, no. 7553, pp. 436–444, 2015.

31. K. Taira, S. L. Brunton, S. Dawson, C. W. Rowley, T. Colonius, B. J. McKeon, O. T. Schmidt, S. Gordelyev, V. Theofilis, and L. S. Ukeiley, "Modal analysis of fluid flows: An overview," *AIAA*, vol. 55, no. 12, pp. 4013–4041, 2017.
32. M. O. Williams, C. W. Rowley, and I. G. Kevrekidis, "A Kernel-Based Approach to Data-Driven Koopman Spectral Analysis," *ArXiv e-prints*, Nov. 2014.
33. S. C. Puligilla and B. Jayaraman, "Deep multilayer convolution frameworks for data-driven learning of fluid flow dynamics," in *24th AIAA Fluid Dynamics Conference, Aviation Forum*, no. 3628, pp. 1–22, 2018.
34. S. E. Otto and C. W. Rowley, "Linearly-recurrent autoencoder networks for learning dynamics," *arXiv preprint arXiv:1712.01378*, 2017.
35. B. Lusch, J. N. Kutz, and S. L. Brunton, "Deep learning for universal linear embeddings of nonlinear dynamics," *arXiv preprint arXiv:1712.09707*, 2017.
36. K. Hornik, M. Stinchcombe, and H. White, "Multilayer feedforward networks are universal approximators," *Neural networks*, vol. 2, no. 5, pp. 359–366, 1989.
37. Y. Bengio, "On the challenge of learning complex functions," *Progress in Brain Research*, vol. 165, pp. 521–534, 2007.
38. B. Schölkopf and A. J. Smola, *Learning with kernels: support vector machines, regularization, optimization, and beyond*. MIT press, 2001.
39. G. H. Golub and C. F. Van Loan, *Matrix computations*, vol. 3. JHU Press, 2012.
40. A. Roshko, "On the development of turbulent wakes from vortex streets," *NACA rep*, 1954.
41. C. Williamson, "Oblique and parallel modes of vortex shedding in the wake of a circular cylinder at low reynolds numbers," *Journal of Fluid Mechanics*, vol. 206, pp. 579–627, 1989.
42. C. D. Cantwell, D. Moxey, A. Comerford, A. Bolis, G. Rocco, G. Mengaldo, D. De Grazia, S. Yakovlev, J.-E. Lombard, D. Ekelschot, *et al.*, "Nektar++: An open-source spectral/hp element framework," *Computer Physics Communications*, vol. 192, pp. 205–219, 2015.
43. E. Weinan and C.-W. Shu, "Small-scale structures in boussinesq convection," *Physics of Fluids*, 1998.
44. J.-G. Liu, C. Wang, and H. Johnston, "A fourth order scheme for incompressible boussinesq equations," *Journal of Scientific Computing*, vol. 18, no. 2, pp. 253–285, 2003.
45. O. San and J. Borggaard, "Principal interval decomposition framework for pod reduced-order modeling of convective boussinesq flows," *International Journal for Numerical Methods in Fluids*, vol. 78, no. 1, pp. 37–62, 2015.
46. S. Pan and K. Duraisamy, "Long-time predictive modeling of nonlinear dynamical systems using neural networks," *arXiv preprint arXiv:1805.12547*, 2018.